J. Fluid Mech. (2004), *vol.* 504, *pp.* 99–132.
DOI: 10.1017/S0022112003007687 Printed in the United Kingdom

Thermocapillary flows under an inclined temperature gradient

By OLEG E. SHKLYAEV† AND ALEXANDER A. NEPOMNYASHCHY

Department of Mathematics, Technion – Israel Institute of Technology, Haifa, 32000, Israel

(Received 7 April 2003 and in revised form 6 October 2003)

The subject of the paper is the stability of the thermocapillary flow generated by an inclined temperature gradient. The investigation is carried out for water (Prandtl number $Pr = 7$) in the limit of a vanishing Biot number. By means of the linear stability analysis, the instability boundary of the return flow and the main instability modes have been found. The evolution of the convective regimes predicted by the linear stability theory and arising as a result of a nonlinear interaction has been studied by a numerical simulation of three-dimensional governing equations. Hexagonal cells differently oriented with respect to the main flow have been revealed as well as roll-like and quadrangular patterns. Transitions between different convective patterns occurring under changes of the governing parameters have been considered.

1. Introduction

Thermocapillary convective flows play the main role in shallow layers and under microgravity conditions when other sources of convection turn out to be negligible. The investigation of thermocapillary flows is a rapidly developing field that has a wide spectrum of applications in engineering (microfluidics, crystal growth processes, chemical engineering, coating, drying etc.). The investigation and prediction of possible convective regimes is important for many natural and technological processes.

There are many works devoted to the investigation of thermocapillary convection in a planar liquid layer. However, most of them consider either the case of heating across the layer or the case of heating along the free surface. In the former case, we observe a sequence of transitions between different convective patterns (for a review see, e.g. Colinet, Legros & Velarde 2001; Nepomnyashchy, Velarde & Colinet 2001*b*). In the latter case, the temperature gradient directed along the free surface generates a thermocapillary flow. The stability of the thermocapillary convection caused by the horizontal temperature gradient was considered by Smith & Davis (1983*a*, *b*), Smith (1986) and Davis (1987) in the framework of the linear theory approach (see also Smith 1988; Kuhlmann 1999). Besides longitudinal rolls, the existence of oblique hydrothermal waves travelling upstream was predicted. The results of the linear stability analysis were justified by the numerical simulations (Xu & Zebib 1998). The weakly nonlinear analysis of the hydrothermal waves was carried out by Smith (1988). The stability of a parallel flow produced by the combined action of

† Present address: Department of Engineering Sciences and Applied Mathematics, Northwestern University, 2145 Sheridan Road, Evanston, Illinois, 60208, USA.

the thermocapillary effect and buoyancy was also investigated in detail (Parmentier, Regnier & Lebon 1993; Priede & Gerbeth 1997).

Note that, in reality, it is difficult to guarantee that the temperature gradient is directed strictly perpendicularly to the layer surface. It is reasonable to consider the situation when the temperature gradient is inclined with respect to the surface. This case is still much less explored. In our opinion, the influence of the longitudinal temperature gradient on the arising convective structures has not yet been understood, nor has the influence of the transverse temperature gradient on the stability of thermocapillary flows.

In the case of the buoyancy convection, Weber (1978) considered the instability of the convective shear flow under the action of an inclined temperature gradient, using the linear stability approach. He found that depending on the horizontal and vertical temperature gradient components, the flow lost its stability with respect to disturbances having different forms. Specifically, longitudinal rolls aligned along the basic flow, transverse travelling rolls and their oscillations, were predicted.

In the case of thermocapillary convection, some estimates that provide relations between critical longitudinal and transverse temperature gradients in the case of the linear flow have been obtained by Davis (1987). Nepomnyashchy, Simanovskii & Braverman (2001*a*) considered the two-layer return thermocapillary flow in the presence of an inclined temperature gradient. They found three instability modes by means of the stability analysis, and performed two-dimensional nonlinear simulations. The supercritical flow regimes in a layer with an inclined temperature gradient have been studied in experiments by Ueno, Kurosawa & Kawamuro (2002). Hosoi & Bush (2001) investigated evaporation-driven convection and studied the stability of a solutocapillary flow in the presence of an inclined concentration gradient.

The goal of this paper is to clarify the action of the inclined temperature gradient on the stability of a thermocapillary return flow and to study the three-dimensional secondary convective regimes. The investigation is carried out for water (Prandtl number $Pr = 7$) in the limit of a vanishing Biot number.

In § 2, the formulation of the problem and governing equations are presented. Section 3 contains a linear stability analysis of the problem. In § 4, we investigate the influence of a horizontal component of the temperature gradient on the convective patterns near the instability threshold. In § 5, we give a brief description of the numerical technique used for solving the governing equations. Section 6 is devoted to the discussion of the results obtained by the numerical simulation.

2. Formulation of the problem

The system under consideration is the infinite plane layer of the viscous incompressible liquid (figure 1). The liquid layer is characterized by the thickness d, kinematic viscosity ν, thermal diffusivity κ, density ρ and surface tension coefficient which linearly depends on the temperature, $\sigma = \sigma_0 - \gamma T$. The buoyancy is neglected, and we assume that the thermocapillary force is the only force capable of initiating the fluid motion. One boundary of the layer is assumed to be rigid, and it is maintained at temperature $T(x) = T_b + \tilde{A}x$ varied along the layer in the horizontal direction. The other boundary represents a free undeformable surface, where the thermocapillary force acts. The presence of the horizontal temperature gradient makes the motionless state of the liquid impossible and the flow along the layer appears.

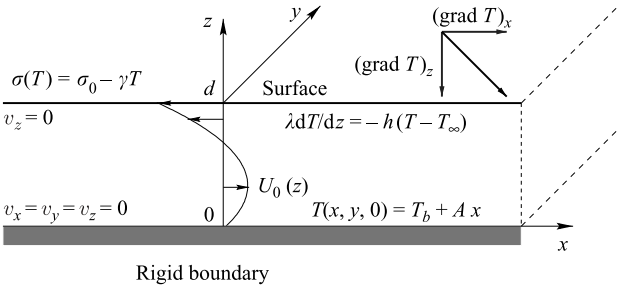

FIGURE 1. Geometry of the system.

The fluid dynamics is governed by the Navier–Stokes system, heat conductivity and continuity equations:

$$\left.\begin{gathered}\partial_t \boldsymbol{v} + (\boldsymbol{v}\cdot\nabla)\boldsymbol{v} = -\frac{\nabla p}{\rho} + \nu\nabla^2\boldsymbol{v},\\ \partial_t T + (\boldsymbol{v}\cdot\nabla)T = \kappa\nabla^2 T,\\ \nabla\cdot\boldsymbol{v} = 0,\\ -\infty < x < \infty, \quad -\infty < y < \infty, \quad 0 < z < d.\end{gathered}\right\} \tag{1}$$

It is also required that the following boundary conditions should be met:

$$\left.\begin{gathered}z = 0\colon \quad v_x = 0, \quad v_y = 0, \quad v_z = 0, \quad T = T_b + \tilde{A}x,\\ z = d\colon \quad \rho\nu\partial_z v_x = -\gamma\,\partial_x T, \quad \rho\nu\partial_z v_y = -\gamma\,\partial_y T, \quad v_z = 0, \quad \lambda\partial_z T = -h(T - T_\infty(x)).\end{gathered}\right\} \tag{2}$$

Here, λ is the heat conductivity coefficient, h is the heat transfer coefficient, T_∞ is the temperature of the gas at a large distance from the liquid surface. The vertical component of the velocity equals zero on both boundaries, the no-slip condition for velocity is taken on the bottom boundary and the condition which takes into account the thermocapillary force is set on the surface. We also define linear distribution of temperature on the bottom, and the law of heat transfer on the top boundary. We shall assume that $T_\infty(x) = \tilde{T} + \tilde{A}x$, where $\tilde{T}$ is constant, i.e. $T_\infty(x)$ has the same horizontal temperature gradient as the temperature field on the rigid boundary $z = 0$.

Turning to the dimensionless variables, we use the layer thickness d as the length scale, ν/d as the velocity scale, d^2/ν as the time scale, $\rho\nu^2/d^2$ as the pressure scale; $\nu\delta T/\kappa$ is the temperature scale, where $\delta T = hd(T_b - \tilde{T})/(\lambda + h\,d)$ is the difference between the temperatures on the boundaries in the absence of the horizontal temperature gradient, i.e. for the conduction temperature profile. Our system has the following set of dimensionless parameters:

$$Ma = \frac{\gamma\delta T d}{\rho\nu\kappa}, \quad Pr = \frac{\nu}{\kappa}, \quad Bi = \frac{hd}{\lambda}, \quad A = \tilde{A}\frac{d}{Pr\,\delta T},$$

which are Marangoni number, Prandtl number, Biot number and dimensionless horizontal temperature gradient, respectively.

Taking into account two components of the applied temperature gradient, it is convenient to present the temperature field in the following way:

$$\frac{T(x, y, z, t) - T_b}{Pr\,\delta T} = \Theta(x, y, z, t) - \frac{z}{Pr} + Ax,$$

where $\Theta(x, y, z, t)$ is the deviation from the linear conductive temperature field. The dimensionless boundary-value problem is as follows:

$$\partial_t \boldsymbol{v} + (\boldsymbol{v}\cdot\nabla)\boldsymbol{v} = -\nabla p + \nabla^2 \boldsymbol{v}, \tag{3}$$

$$\partial_t \Theta + \boldsymbol{v}\cdot\nabla(\Theta - Pr^{-1}z + Ax) = Pr^{-1}\nabla^2\Theta, \tag{4}$$

$$\nabla\cdot\boldsymbol{v} = 0, \tag{5}$$

$$-\infty < x < \infty, \quad -\infty < y < \infty, \quad 0 < z < 1;$$

$$z = 0: \quad v_x = v_y = v_z = 0, \quad \Theta = 0; \tag{6}$$

$$z = 1: \quad \partial_z v_x = -Ma\,\partial_x\Theta, \quad \partial_z v_y = -Ma\,\partial_y\Theta, \quad v_z = 0, \quad \partial_z\Theta = -Bi\Theta. \tag{7}$$

The problem (3)–(6) has an exact solution corresponding to a parallel return flow (see Smith & Davis 1983*a*; Birikh 1966)

$$\left.\begin{aligned} &v_x = U_0(z) = \tfrac{1}{2}Ma\,A(z - 1.5z^2), \quad v_y = v_z = 0,\\ &\Theta_0(z) = \tfrac{1}{4}Ma\,A^2 Pr\left(\tfrac{1}{3}z^3 - \tfrac{1}{4}z^4\right) - \frac{Ma\,A^2 Pr\,Bi}{48(Bi+1)}z,\\ &p = Bx = -\tfrac{3}{2}Ma\,Ax. \end{aligned}\right\} \tag{8}$$

The term 'return flow' means that the fluid flux along the layer vanishes:

$$\int_0^1 U_0(z)\,\mathrm{d}z = 0.$$

3. Linear stability analysis

In the present section, we develop the linear stability theory of the flow (8). This theory suggests some predictions as to the arising convective regimes. It gives the stability boundary of the return flow with respect to the disturbances in the form of rolls and travelling waves.

Unlike the case of zero temperature gradient A, owing to the anisotropy of the problem under consideration there is a certain preferred direction along which the perturbations grow most rapidly. This direction can be inclined with respect to the direction of the main return flow. In order to find this direction, it is necessary to calculate the marginal stability surface. Stability analysis has been performed in this paper similarly to the analysis given by Nepomnyashchy *et al.* (2001*a*) for a two-layer system.

To study the stability of the return flow we linearize the system defined by (3)–(6) around the stationary solution (8), and assume that the infinitesimal disturbances form a normal mode. Also we perform the transformation of coordinates $x = X\cos(\alpha) + Y\sin(\alpha)$, $y = -X\sin(\alpha) + Y\cos(\alpha)$, assuming that $k_x = k\sin(\alpha)$, $k_y = k\cos(\alpha)$, where $\boldsymbol{k} = (k_x, k_y)$. After that transformation, the vector $\boldsymbol{k}$ becomes directed along the Y-axis and the disturbances do not depend on X. Now the basic flow and perturbations of the variables have the following form:

$$\begin{aligned} \Theta &= \Theta_0(z) + AX\cos(\alpha) + AY\sin(\alpha) + \tilde{\theta}(z)\exp(\mathrm{i}kY + \lambda t),\\ p &= BX\cos(\alpha) + BY\sin(\alpha) + \tilde{p}(z)\exp(\mathrm{i}kY + \lambda t),\\ v_X &= U_0(z)\cos(\alpha) + \tilde{v_X}(z)\exp(\mathrm{i}kY + \lambda t),\\ v_Y &= U_0(z)\sin(\alpha) + \tilde{v_Y}(z)\exp(\mathrm{i}kY + \lambda t),\\ v_z &= \tilde{v_z}(z)\exp(\mathrm{i}kY + \lambda t). \end{aligned}$$

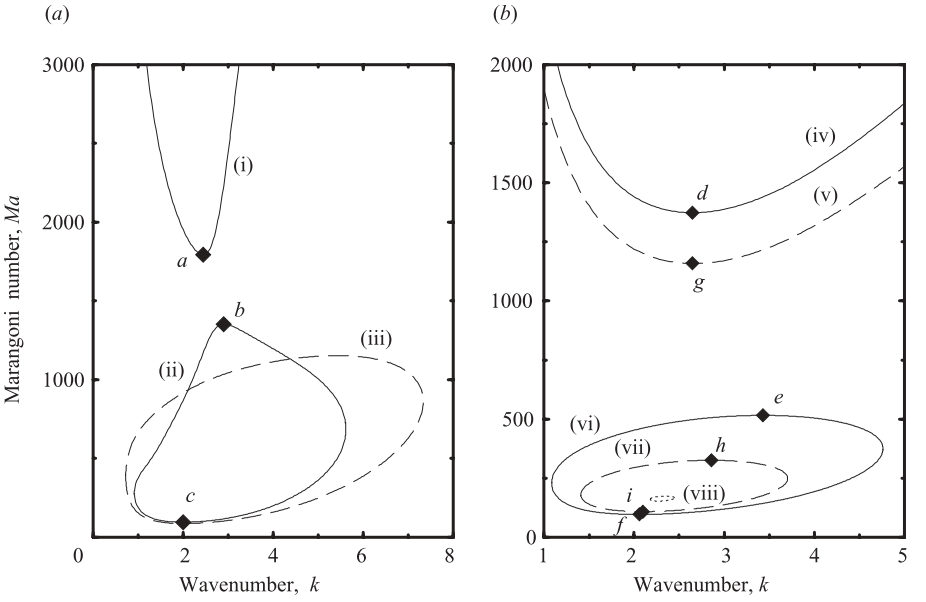

FIGURE 2. (*a*) marginal curves at $A = 0.022$ for travelling rolls with $\alpha = 90°$, (lines (i), (ii)) and for stationary rolls with $\alpha = 0°$ (line (iii)); (*b*) marginal curves for hydrothermal waves ($A = 0.03$, line (iv); $A = 0.035$, line (v)) and for stationary rolls with $\alpha = 0°$ ($A = 0.03$, line (vi); $A = 0.035$, line (vii); $A = 0.0398$, line (viii)).

The continuity equation $\mathrm{i}k\tilde{v_Y}(z) + \tilde{v_z'}(z) = 0$ makes it possible to introduce the stream-function $\tilde{v_z} = -\mathrm{i}k\psi$, $\tilde{v_Y} = \psi'$ for the flow in the (Y, z)-plane. We obtain the following eigenvalue problem describing the stability of the return flow (the tilde is omitted):

$$\left.\begin{aligned} &(\psi'''' - 2k^2\psi'' + k^4\psi) - \mathrm{i}k\sin(\alpha)[U_0(\psi'' - k^2\psi) - \psi U_0''] - \lambda(\psi'' - k^2\psi) = 0, \\ &\lambda v_X + \mathrm{i}kU_0\sin(\alpha)v_X - \mathrm{i}k\psi U_0'\cos(\alpha) = v''_X - k^2 v_X, \\ &\lambda\theta + v_X A\cos(\alpha) + \mathrm{i}kU_0\psi'\sin(\alpha)\sin(\alpha)\theta - \mathrm{i}k\psi\theta'_0 = Pr^{-1}(\theta'' - k^2\theta - \mathrm{i}k\psi); \end{aligned}\right\} \quad (9)$$

$$\left.\begin{aligned} &z = 1: \quad v'_X = \psi = \psi'' + Ma\,\mathrm{i}k\,\theta = \theta' + Bi\,\theta = 0, \\ &z = 0: \quad v_X = \psi = \psi' = \theta = 0. \end{aligned}\right\} \quad (10)$$

The eigenvalue problem is solved in the following way. The eigenfunction is constructed as a linear combination of the linearly independent solutions of (9) and (10) satisfying the boundary conditions at $z = 0$. The solutions are found numerically using the Runge–Kutta integration scheme. The boundary conditions at $z = 1$ lead to a linear homogeneous algebraic system which has non-trivial solutions if the real and the imaginary parts of its determinant $D(\lambda; k, Ma, Pr, Bi) = D_r + \mathrm{i}D_i$ vanish. The conditions $D_r = D_i = 0$ determine the real and the imaginary parts of the eigenvalue λ as function of other parameters. Actually, for fixed values of k, Pr and Bi we search the marginal value of Ma such that the eigenvalue λ is purely imaginary, $\lambda = \mathrm{i}\omega$. The values of ω and Ma that ensure $D_r = D_i = 0$ are found by the Newton method. The computation has been done with $Pr = 7$ and $Bi = 0$.

In order to investigate the stability of the flow, first we have to obtain the marginal curves $Ma(k)$ corresponding to fixed values of the angle α and of the horizontal temperature gradient A. The results correspond to different kinds of instabilities. The marginal curves can contain disconnected and closed fragments. Some typical examples of marginal curves are shown in figure 2. Curves (i) and (ii) in figure 2(*a*) are drawn

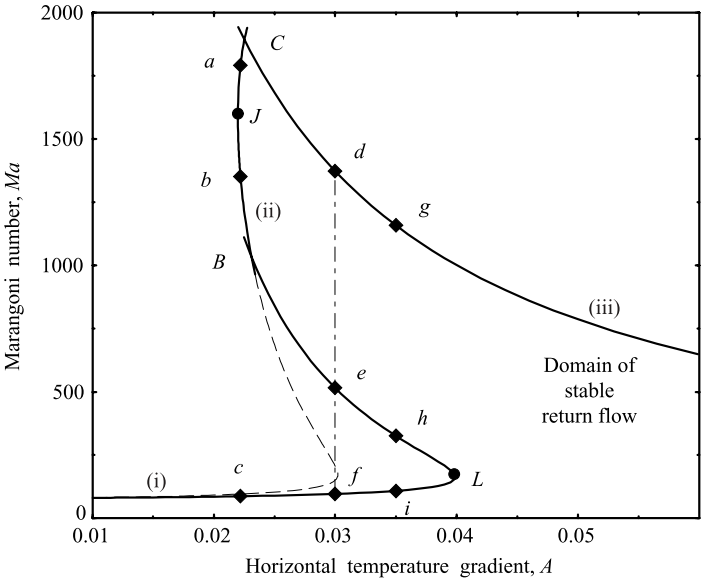

FIGURE 3. Map of the return flow stability. Solid lines: (i) instability boundary with respect to stationary longitudinal rolls $\alpha = 0°$, up to B; (ii) travelling rolls with $\alpha = 90°$, between the points B and C; (iii) oblique hydrothermal waves $\alpha = \alpha_c$, from the point C and further to the right. Dashed line: instability boundary of travelling rolls with $\alpha = 90°$ in the region where the instability is caused by the longitudinal rolls. Points $a - l$ correspond to the same points in figure 2.

at the value of the horizontal temperature gradient $A = 0.022$ for travelling rolls with $\alpha = 90°$. Curve (iii) is the instability boundary of the stationary longitudinal rolls with $\alpha = 0°$. Both curve (iv) corresponding to the oblique hydrothermal wave with $\alpha = \alpha_c(A)$, which provides the lowest minimum value of Ma, and curve (vi) corresponding to the stationary longitudinal rolls, in figure 2(b) have been obtained at the value of the horizontal temperature gradient at $A = 0.03$. Curve (v) (oblique hydrothermal wave), and curve (vii) (stationary longitudinal rolls) present the corresponding instability boundaries at $A = 0.035$. Curve (viii) is the marginal curve for stationary longitudinal rolls at $A = 0.0398$. The instability domain is contained inside the closed curves (ii) and (iii) of figure 2(a) and curves (vi), (vii) and (viii) of figure 2(b). Then we find the maximum and the minimum points of marginal curves (critical Marangoni numbers) corresponding to different kinds of instabilities (e.g. points c and b on curve (ii), figure 2a and points f, i, h, e on curves (vii) and (viii) of figure 2b) and construct the full stability diagram of the return flow (see figure 3) in the plane of parameters (Ma_c, A, critical Marangoni number versus horizontal temperature gradient).

Figures 2 and 3 mutually correspond to each other. The minimum and maximum points in figure 2 belong to various parts of the whole instability boundary in figure 3. All the curves in figure 3 presenting the instability boundary of the return flow have already been minimized with respect to the angle α and the wavenumber k_c.

Curve (i) in figure 3 presents the instability boundary for longitudinal rolls $\alpha = 0°$ (solid line). At point B, this curve crosses the instability boundary for travelling rolls with $\alpha = 90°$. Below point B, the instability boundary for rolls with $\alpha = 90°$ is shown as a dashed line. Instability boundaries for other modes having arbitrary angles $0° < \alpha < 90°$ are located inside the instability region. Below point B, the return

flow instability is first produced by the longitudinal rolls. As the horizontal gradient approaches point $A=0$, minima of marginal curves for different α merge at the point $Ma_c=79.6$, $k_c=2$ which corresponds to the result of Pearson (1958).

Curve (ii) in figure 3 between points B and C is the instability boundary for the travelling rolls with $\alpha=90°$. Point J is the extreme left point of this boundary. We can see that for horizontal gradient values less then A_J (corresponding to the point J in figure 3), instability occurs for any point above line (i). For values in the range $A_J<A<A_L$, there is a gap of stability for a parallel flow. In this range, the transition to the convection occurs in different ways, depending on A. As an example, consider the section at $A=0.03$ (dot-dashed line between the points d and f in figure 3). If we enhance Ma maintaining the constant value of A, then, at $Ma=Ma_f$, the parallel flow becomes unstable with respect to the stationary longitudinal rolls (point f on curve (vi), figure 2*b*). With the further increase of the temperature difference across the layer, the parallel flow is restabilized at $Ma=Ma_e$ (point e in figure 3 and point e on curve (vi), figure 2*b*) and remains stable up to $Ma=Ma_d$ (point d, figure 3 and point d on curve (iv), figure 2*b*). Here the flow loses stability with respect to inclined hydrothermal waves with $\alpha\neq0$ moving upstream. In figures 3 and 2(*a*) also, points a, b and c are shown presenting the section at $A=0.022$ under increasing Marangoni number and fixed temperature gradient. The analogous points g, h and i present the section at $A=0.035$ in figures 3 and 2(*b*). The shape of the instability boundary shows that for temperature gradient values exceeding A_L, Pearson's instability mechanism is suppressed and transition to convection occurs through hydrothermal waves only. This instability boundary (curve (iii) in figure 3) is plotted for the angle $\alpha=\alpha_c$, which minimizes the critical Marangoni number. This curve starts from point C and continues up to infinity, $A\to\infty$. The critical angle α_c at point C is $\alpha_c=31°$ at points d and g it is 37.4° and 40.1°, respectively, and at the point where $A=0.06$ it is $\alpha_c=47.1°$.

Summarizing the results of the linear stability analysis, we can see that for relatively small values of the horizontal temperature gradient, Pearson's instability mechanism takes place and stationary convective rolls appear. The axes of these rolls are ordered along the basic flow. The instability boundary of this mode starts from the point with zero temperature gradient and extends to point B, where the instability boundary turns into another mode which corresponds to the rolls ordered perpendicularly to the direction of the basic flow. These rolls move in the direction of the flow on the surface, thus they are travelling rolls. At point C and further on in the direction of increasing horizontal temperature gradient, the instability with respect to oblique hydrothermal waves becomes most dangerous. These waves propagate in the direction opposite to the direction of the flow on the surface. The latter kind of instability was investigated by Smith & Davis (1983*a*) in the limit $1/A\to0$.

One of the shortcomings of the linear theory is that it cannot predict patterns different from rolls. It is known that, in the absence of the horizontal gradient of the temperature A, the hexagonal cells are the first patterns which appear from the motionless state. We can expect that this kind of pattern may develop at least for sufficiently small values of the horizontal temperature gradient A. Also, the linear theory is unable to predict the type of bifurcation (supercritical or subcritical).

4. Weakly nonlinear regimes

In the present section, we shall consider the weakly nonlinear regimes of convection under the action of a small horizontal temperature gradient A. First, let us discuss the

linear growth of disturbances. In the absence of the horizontal temperature gradient $A=0$, the growth rate of the disturbances is real and does not depend on the direction of the wavenumber $\boldsymbol{k}$: $\sigma=\sigma(k^2)$. When the temperature gradient $A\,\boldsymbol{e}_x$ is applied, the function $\sigma=\sigma(\boldsymbol{k}, A\boldsymbol{e}_x)$ is complex and it can be presented as a function of scalar invariants k^2, $A\boldsymbol{k}\cdot\boldsymbol{e}_x$, A^2. Taking into account the relation $\sigma(\boldsymbol{k}, A\boldsymbol{e}_x)=\sigma^*(-\boldsymbol{k}, A\boldsymbol{e}_x)$, which can be established from the analysis of the linearized problem, we find that for small A

$$\sigma_r(\boldsymbol{k}, A\boldsymbol{e}_x)=\sigma_r^{(0)}(k^2)+A^2\left[\sigma_1^{(2)}(k^2)+\sigma_2^{(2)}(k^2)(\boldsymbol{k}\cdot\boldsymbol{e}_x)^2\right]+O(A^4), \tag{11}$$

$$\sigma_i(\boldsymbol{k}, A\boldsymbol{e}_x)=A(\boldsymbol{k}\cdot\boldsymbol{e}_x)\sigma_1^{(1)}(k^2)+O(A^3). \tag{12}$$

Let us consider now the weakly nonlinear regimes. It is well known that in the case $A=0$, a hexagonal pattern is developed near the instability threshold (Palm 1960) which is described by three amplitudes a_1, a_2, a_3 corresponding to wave vectors $\boldsymbol{k}_1$, $\boldsymbol{k}_2$, $\boldsymbol{k}_3$, $|\boldsymbol{k}_j|=k_c$, $j=1, 2, 3$; $\boldsymbol{k}_1+\boldsymbol{k}_2+\boldsymbol{k}_3=0$. Let us consider the hexagonal pattern at $A\neq 0$. Under the assumption of weak quadratic interaction, the nonlinear evolution of amplitudes can be described by a simple model system of amplitude equations which contains both quadratic and cubic coefficients (Scanlon & Segel 1967):

$$\partial_t a_1=\sigma(\boldsymbol{k}_1, A)a_1+\delta a_2^* a_3^*-|a_1|^2 a_1-\kappa(|a_2|^2+|a_3|^2)a_1.$$

The other equations are obtained by a cyclic permutation of the subscripts 1, 2, 3. To leading order, small A does not influence the coefficients of the nonlinear interaction, but we have to take into account the dependence of the growth rate on A, which will be presented as follows,

$$\sigma(\boldsymbol{k}_j, A)=\Gamma+\mathrm{i}\alpha(\boldsymbol{k}_j\cdot\boldsymbol{e}_x)A-\beta(\boldsymbol{k}\cdot\boldsymbol{e}_x)^2A^2,$$

where $\Gamma=\sigma_r^{(0)}(k^2)+A^2\sigma_1^{(2)}(k^2)$, $\alpha=\sigma_1^{(1)}(k^2)$ and $\beta=-\sigma_2^{(2)}(k^2)$. According to the results of the previous section, $\beta>0$, i.e. the disturbance with the wavevector orthogonal (i.e. the roll axis parallel) to the direction of the horizontal temperature gradient A (longitudinal rolls) has a larger growth rate than the disturbance with the wave vector along (i.e. the roll axis across) that direction (transverse rolls). It is remarkable that because of the condition $\boldsymbol{k}_1+\boldsymbol{k}_2+\boldsymbol{k}_3=0$, the imaginary part of the growth rate can be fully eliminated by the transformation

$$a_j=a_j'\exp(\mathrm{i}\alpha(\boldsymbol{k}_j\cdot\boldsymbol{e}_x)A\,t).$$

Omitting the prime, we obtain the amplitude equation:

$$\partial_t a_1=\Gamma_1 a_1+\delta a_2^* a_3^*-|a_1|^2 a_1-\kappa(|a_2|^2+|a_3|^2)a_1, \quad \Gamma_1=\Gamma-\beta(\boldsymbol{k}_1\cdot\boldsymbol{e}_x)^2A^2.$$

Other equations can be obtained by the permutation of subscripts. Note that the system of amplitude equations for perfect hexagons ($|\boldsymbol{k}_j|=k_c$) in the presence of a horizontal temperature gradient A is formally equivalent to the system of amplitude equations for non-equilateral hexagons ($|\boldsymbol{k}_j|\neq k_c$, but $\boldsymbol{k}_1+\boldsymbol{k}_2+\boldsymbol{k}_3=0$) studied by Malomed, Nepomnyashchy & Nuz (1994).

As a basic example, let us consider the hexagonal pattern with the angles between $\boldsymbol{k}_j$ and $\boldsymbol{e}_x$ equal to 90°, 210° and −30° (pattern $H1$, see figure 14). Rescale the variables in the following way: $a_j=\bar{a}_j\delta$, $j=1, 2, 3$, $\Gamma=\gamma\delta^2$, $\partial_t=\delta^2\partial_{\bar{t}}$, $\beta A^2=\bar{A}^2\delta^2$. Omitting the

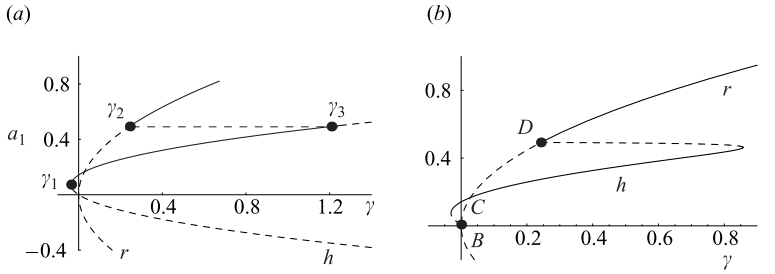

FIGURE 4. Bifurcation diagram for the cases (*a*) $\bar{A}=0$, $\kappa=3$, $\beta=1$; (*b*) $\bar{A}=0.1$, $\kappa=3$, $\beta=1$. Solid (dashed) lines correspond to stable (unstable) patterns.

bar sign over $\bar{a}_j$, the system of the amplitude equations is written as follows:

$$\left.\begin{aligned}
\partial_t a_1 &= \gamma a_1 + a_2^* a_3^* - |a_1|^2 a_1 - \kappa(|a_2|^2 + |a_3|^2)a_1,\\
\partial_t a_2 &= \gamma a_2 + a_1^* a_3^* - |a_2|^2 a_2 - \kappa(|a_1|^2 + |a_3|^2)a_2 - \tfrac{3}{4}\bar{A}^2 a_2,\\
\partial_t a_3 &= \gamma a_3 + a_1^* a_2^* - |a_3|^2 a_3 - \kappa(|a_1|^2 + |a_2|^2)a_3 - \tfrac{3}{4}\bar{A}^2 a_3.
\end{aligned}\right\} \tag{13}$$

Later on, we shall assume that amplitudes a_j are real; that corresponds to the correlation of phases, typical for hexagonal patterns. System (13) has many stationary solutions. The solution $a_1=a_2=a_3=0$ corresponds to the trivial state of the parallel flow. Solutions $a_1=\sqrt{\gamma}$, $a_2=a_3=0$; $a_2=\sqrt{\gamma-3/(4\bar{A}^2)}$, $a_1=a_3=0$ and $a_3=\sqrt{\gamma-3/(4\bar{A}^2)}$, $a_1=a_2=0$ correspond to stationary rolls of different orientation. The solutions with all the amplitudes different from zero correspond to hexagonal patterns. For the sake of simplicity, we shall term as 'hexagonal pattern' the pattern with all the amplitudes a_1, a_2 and a_3 different from zero, though the actual shape of this pattern can be rather different from the usual hexagons if $a_1 \neq a_2$ (see Malomed *et al.* 1994).

In the absence of the horizontal temperature gradient ($\bar{A}=0$ in (13)), the behaviour of the solutions and competition between hexagons and rolls are well known and shown in figure 4(*a*). Line *r* presents the roll solution with $\gamma - a_1^2 = 0$ and $a_2=a_3=0$; line *h* presents the hexagons described by the relations $\gamma = a_1^2(1+2\kappa) - a_1$ and $a_1=a_2=a_3$. Hexagonal patterns appear in a subcritical way and are stable within the interval

$$\gamma_1 = -\frac{1}{4(1+2\kappa)} < \gamma < \gamma_3 = \frac{\kappa+2}{(\kappa-1)^2}.$$

The roll solutions are stable for γ larger then $\gamma_2 = 1/(\kappa-1)^2$. As $\gamma > \gamma_2$, there is also an unstable solution with $a_1 = 1/(\kappa-1)$ and $a_2=a_3\neq 0$ which connects branches of hexagonal patterns and rolls (dashed line in figure 4*a*, black dots correspond to γ_1, γ_2 and γ_3). We can see that there are two multistability domains. The first is located within the interval $\gamma_1 < \gamma < 0$ where the parallel return flow and the hexagons are stable; the second one is within the interval

$$\gamma_2 < \gamma < \gamma_3,$$

where depending on the initial conditions, we can obtain a hexagonal pattern or rolls as $t \to \infty$. In these domains, hysteretical transitions are possible with the change of γ.

Let us consider now the case with the horizontal temperature gradient different from zero, $\bar{A}\neq 0$ in (13) (figure 4*b*). The orientation of the wave vector across the direction of gradient $\bar{A}$ is preferable and this circumstance leads to a distortion of the hexagonal structure. Because of the symmetry of system (13), there exists a class

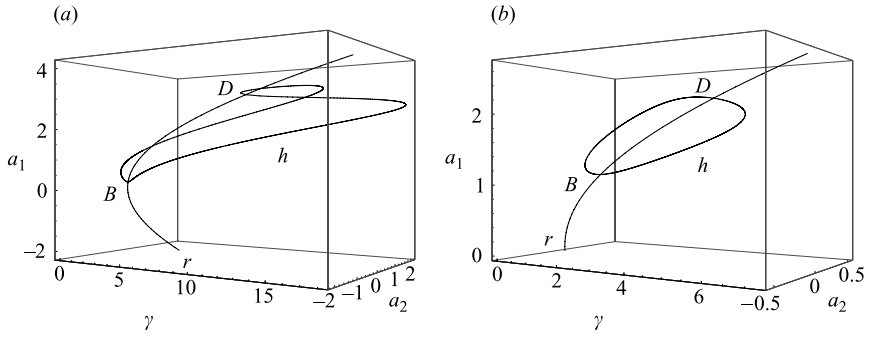

FIGURE 5. Amplitude branches for cases (*a*) $\bar{A}=0.5$, $\kappa=1.3$, $\beta=1$; (*b*) $\bar{A}=0.999$, $\kappa=1.3$, $\beta=1$.

of solutions with $a_1 \neq a_2 = a_3$, for which the stationary system (13) reads

$$\gamma a_1 + a_2^2 - a_1^3 - 2\kappa a_2^2 a_1 = 0,$$
$$\gamma - \tfrac{3}{4}\bar{A}^2 + a_1 - a_2^2 - \kappa\left(a_1^2 + a_2^2\right) = 0.$$

These two equations can be rewritten as

$$a_2^2 = \frac{\gamma a_1 - a_1^3}{2\kappa a_1 - 1}, \tag{14}$$

$$\gamma + a_1 - \frac{\gamma a_1 - a_1^3}{2\kappa a_1 - 1}(1+\kappa) - \kappa a_1^2 - \tfrac{3}{4}\bar{A}^2 = 0. \tag{15}$$

Typical amplitude curves in the space (a_1, a_2, γ) are shown in figure 5. Typical projections of these curves onto the planes (a_1, γ) and (a_2, γ) are shown in figures 4(*b*) and 6. We can see that unlike the case of $\bar{A}=0$, the amplitude curve a_1 of the hexagonal patterns (lines h) bifurcates from the amplitude curve of the roll (lines r) at point B (which does not coincide with the origin) and at point D. The projections of the lines h and r onto the plane (a_1, γ) (see figure 4*b* and the right-hand column in figure 6) can cross at point C. We can see that at relatively small values of $\bar{A}$ different from zero, both the multistability domains mentioned above remain. However, now, the first domain (to the left of point B) can contain, besides stable hexagonal patterns, both the stable parallel return flow (on the interval of the γ-axis under curve h, to the left of point B in figure 4*b*) and the stable roll solutions (on curve r under branch h to the left of point B in figure 6(*b*) depending on the value of $\bar{A}$, which deforms the hexagonal branch h. Note that hexagons are stable only in the part of curve h where $\partial a_2/\partial\gamma > 0$. For more detail about the stability of hexagonal patterns governed by the amplitude equations (13), see Malomed *et al.* (1994).

Let us discuss the change of the hexagonal branch h which occurs with the change of the temperature gradient $\bar{A}$. Consider the bifurcation of the hexagonal pattern from the rolls in more detail. We expand all the variables in (14) around the roll solution:

$$a_2 = \varepsilon a_2^{(1)} + \varepsilon^2 a_2^{(2)} + \cdots,$$
$$a_1 = \sqrt{\gamma_0} + \varepsilon a_1^{(1)} + \varepsilon^2 a_1^{(2)} + \cdots,$$
$$\gamma = \gamma_0 + \varepsilon\gamma_1 + \varepsilon^2\gamma_2 + \cdots.$$

In the zeroth order in ϵ, we can find two bifurcation points

$$\sqrt{\gamma_0}_{\pm} = \frac{1 \pm \sqrt{1-(\kappa-1)3\bar{A}^2}}{2(\kappa-1)},$$

where the hexagonal pattern with $a_2 = a_3 \neq 0$ appears from the roll solution $a_1 = \sqrt{\gamma_0}$. In the second order in ϵ, we can obtain the correction $[a_2^{(1)}]^2 = \gamma_2 P$, where the sign of

$$P = \frac{-2\gamma_0 - \sqrt{\gamma_0} + 2\kappa\gamma_0}{-2\gamma_0(1+\kappa) + (2\kappa\sqrt{\gamma_0} - 1)^2},$$

is responsible for the bifurcation type. We can see that P changes the sign at the point

$$(\sqrt{\gamma_0})_{\pm} = \frac{1}{2\kappa \pm \sqrt{2(1+\kappa)}},$$

which corresponds to the horizontal temperature gradient values

$$\bar{A}_{\pm}^2 = \frac{4}{3}\,\frac{\kappa + 1 \pm \sqrt{2(1+\kappa)}}{2\kappa \pm \sqrt{2(1+\kappa)}}.$$

The sign (+) corresponds to the left bifurcation point B, the sign (−) corresponds to the right point, D. Therefore, we can conclude that for the temperature gradient value $\bar{A} < \bar{A}_+$, the correction P is negative for the left B and right D bifurcation points, and subcritical bifurcations take place there. This is demonstrated in figures 6(*a*) and 6(*b*) where we can see that at the bifurcation point B, $\partial^2\gamma/\partial a_2^2 < 0$ and the hexagonal solution branches off to the left from point B. For the interval $\bar{A}_+ < \bar{A} < \bar{A}_-$, the correction $P > 0$ for the left bifurcation point B. This is the supercritical case and $\partial^2\gamma/\partial a_2^2 > 0$ here (curve h goes to the right from point B, figure 6*c*, points B and C almost merged in figure 6*d*). However, for the right point D, the bifurcation remains subcritical (curve h goes to the right from point D, figure 6*c*, *d*). For the gradient values $\bar{A} > \bar{A}_-$, both points have a supercritical bifurcation type: points B and D in figure 6*e*, *f*. The hexagonal branch h turns out to be stable, whereas the roll branch r is unstable for the values of γ corresponding to the interval between points B and D.

This brief consideration leads to the conclusion that the presence of the horizontal temperature gradient $\bar{A}$ breaks down the symmetry of the problem. The hexagonal patterns typically have amplitudes $a_1 \neq a_2 = a_3$. In a certain region of $\bar{A}$, $\bar{A} > \bar{A}_+$, the first multistability domain for hexagons and return flow or roll patterns disappears; but the second multistability domain remains. Under the temperature gradient increasing beyond the value $\bar{A} = \bar{A}_-$, we can observe the continuous transition between stable rolls and a stable hexagonal pattern. Increasing the horizontal temperature gradient $\bar{A}$, we can remove the region of the hysteretical transitions. We should note that only the first multistability domain is of practical interest because the second domain of the restabilization of rolls is usually outside the validity region of the amplitude equations (13).

5. Numerical method

In this section, we briefly describe the numerical technique used for solving the system of governing equations and boundary conditions (3)–(7). For this purpose, we eliminate the pressure using the decomposition of the velocity field into poloidal Φ

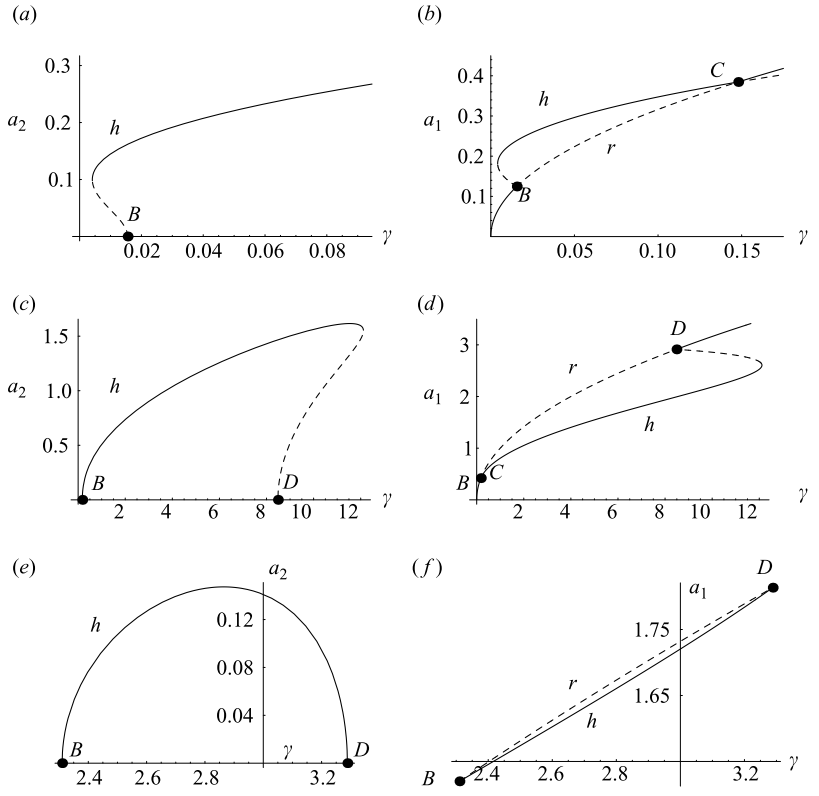

FIGURE 6. Bifurcation diagrams for the cases (a, b) $\bar{A} = 0.4$, $\kappa = 1.3$, $\beta = 1$; (c, d) $\bar{A} = 0.7$, $\kappa = 1.3$; (e, f) $\bar{A} = 1.05$, $\kappa = 1.3$. The left-hand column shows variation of the amplitude a_2. The curves h in the right-hand column present the variation of the amplitude a_1. The curve r is the roll amplitude $a_1 = \sqrt{\gamma}$. Solid (dashed) lines correspond to stable (unstable) patterns.

and toroidal Ψ parts

$$\begin{aligned}\boldsymbol{v}(x, y, z, t) &= \nabla \times (\nabla \times \boldsymbol{e}_z \Phi(x, y, z, t)) + \nabla \times \boldsymbol{e}_z \Psi(x, y, z, t) + U(z)\boldsymbol{e}_x + V(z)\boldsymbol{e}_y \\ &= \left(\Phi_{xz} + \Psi_y + U, \quad \Phi_{yz} - \Psi_x + V, \quad -\nabla_h^2 \Phi\right),\end{aligned}$$

where $U(z)$ and $V(z)$ are the components of the mean flow along the x- and y-directions, respectively. Then the boundary problem (3)–(7) can be presented in the variables of the vertical velocity $v_z = -\nabla_h^2 \Phi$, the vertical vorticity $w_z = -\nabla_h^2 \Psi$, the temperature deviation $\theta(x, y, z, t)$ and the two mean horizontal components of velocity $U(z, t)$ and $V(z, t)$:

$$\left.\begin{aligned}&\partial_t w_z - \boldsymbol{e}_z \cdot \nabla \times (\boldsymbol{v} \times \boldsymbol{w}) = \nabla^2 w_z, \\ &\partial_t \nabla^2 v_z + \partial_z \nabla \cdot (\boldsymbol{v} \times \boldsymbol{w}) - \boldsymbol{e}_z \cdot \nabla^2 (\boldsymbol{v} \times \boldsymbol{w}) = \nabla^4 v_z, \\ &Pr(\partial_t \theta + (\boldsymbol{v} \cdot \nabla)\theta) = \nabla^2 \theta + v_z - Pr\, A v_x, \\ &\partial_t U + \partial_z \langle v_x v_z \rangle^{xy} = \partial_z^2 U - \langle \partial_x p \rangle, \\ &\partial_t V + \partial_z \langle v_y v_z \rangle^{xy} = \partial_z^2 V - \langle \partial_y p \rangle,\end{aligned}\right\} \tag{16}$$

where $\nabla_h^2 = \partial_x^2 + \partial_y^2$ is the horizontal Laplacian, $\langle f \rangle^{xy}$ is the horizontal average of $f(x, y, z)$. System (16) was being solved by using the pseudospectral technique described by Canuto *et al.* (1987) and Boeck (2000). The periodic boundary conditions

$f(x, y, z) = f(x + l_x, y, z)$, $f(x, y, z) = f(x, y + l_y, z)$, were imposed along the two horizontal directions. Conditions on the boundaries of the layer are:

$$\left.\begin{array}{ll} z = 1: & \partial_z^2 v_z - Ma\nabla_h^2\theta = v_z = \partial_z\omega_z = \partial_z\theta + Bi\theta = \partial_z U + MaA = \partial_z V = 0, \\ z = 0: & v_z = \theta = \partial_z v_z = \omega_z = U = V = 0. \end{array}\right\} \quad (17)$$

The conditions of the zero fluid flux, $\int_0^1 U(z)\,\mathrm{d}z = 0$ and $\int_0^1 V(z)\,\mathrm{d}z = 0$, are achieved by adjusting the terms of pressure gradient $\langle\partial_x p\rangle$ and $\langle\partial_y p\rangle$. The solution of the problem (16), (17) is approximated using the presentation of variables $v_z(x, y, z, t)$, $w_z(x, y, z, t)$ and $\theta(x, y, z, t)$ in the series

$$\theta(x, y, z, t) = \sum_{m=-N_x/2}^{N_x/2-1} \sum_{n=-N_y/2}^{N_y/2-1} \sum_{p=0}^{N_z} \widehat{\theta}^{(p,m,n)}(t) T_p(2z - 1) \exp(\mathrm{i}(mk_x x + nk_y y)), \quad (18)$$

where $T_p(2z - 1)$ are Chebyshev polynomials.

All calculations were performed with a constant time step which varied in the range $2 \times 10^{-2} - 10^{-4}$ for different flows. We considered the convective flow as a steady state when the quantity $\epsilon = |f^n - f^{n-1}|/\max(|f^n|, |f^{n-1}|)$ was less than $10^{-6} - 10^{-7}$, depending on the complexity of the regime. Usually, we used the Nusselt numbers as the function f. Typically, it took several dimensionless time units to achieve the steady state; in the vicinity of the bifurcation points, it took, a few dozen time units. We used a computed convective regime as an initial state for the following one that was calculated for other values of the parameters. As a rule, in our simulations, we moved (in the plane of parameters Ma, A) in the direction from the regime with larger amplitude toward the flow with lesser amplitude of the convective motion. Usually, this direction coincided with the direction toward the nearest boundary of the stability domain. In the case of an oscillating convective flow, we carried out averaging quantity f over several time periods.

Details of the code validation are presented in the Appendix.

6. Results of numerical simulation

6.1. *Roll patterns*

We start the consideration of convective regimes with observations of the nonlinear features of the roll patterns that are predicted by the stability analysis developed in § 3. As we have mentioned above, the presence of the horizontal component of the temperature gradient breaks the rotational symmetry of the problem. As a result, we can expect that nonlinear features of the rolls directed along and across the main flow will be different. First, consider the nonlinear competition of these two modes only. For this purpose, we have performed simulations in a computation domain suitable for mutual coexistence of rolls with $\alpha = 0°$ and rolls with $\alpha = 90°$. Spatial scales of the domain were chosen as $l_x = 2\pi/k_x$, $l_y = 2\pi/k_y$ where k_x and k_y were taken on the corresponding marginal curves. The results of calculations are shown in figure 7 where the characteristic forms of the amplitude curves for these two kinds of rolls are presented.

To characterize the intensity of the fluid motion, we chose the following integral characteristics. The first of them is the kinetic energy of the fluid motion based on

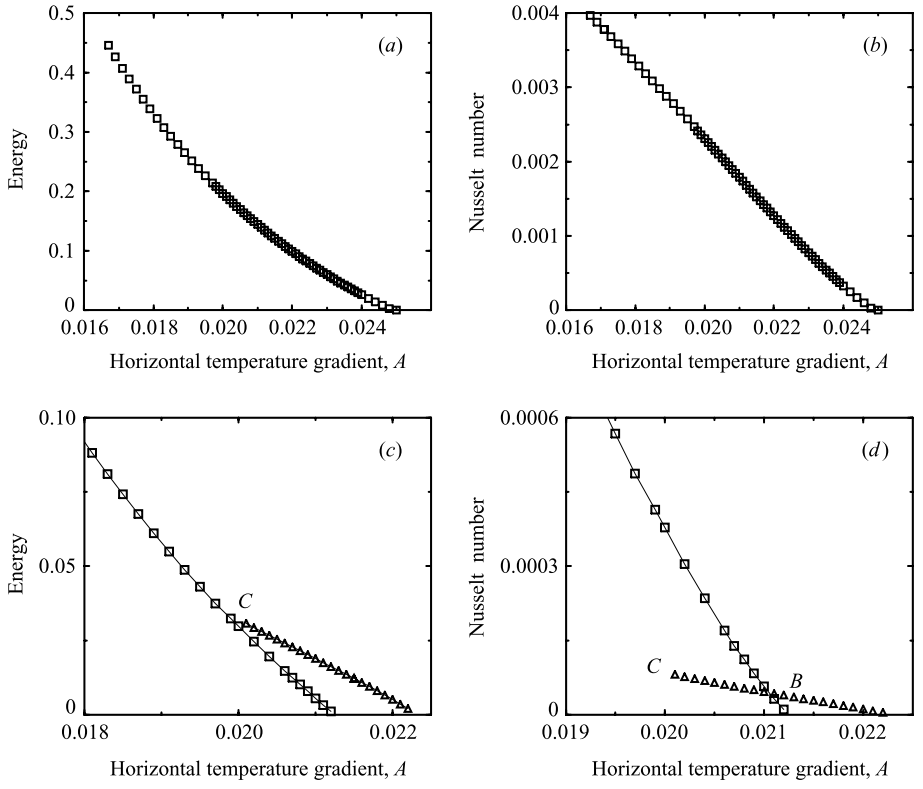

FIGURE 7. The bifurcation diagrams for the rolls. (*a*) Dependence of the energy of the flow on the horizontal gradient A, $\alpha = 0°$, $Ma = 850$; (*b*) dependence of the Nusselt number on the gradient A for the same values of Ma and α (spatial resolution $64 \times 32 \times 32$); (*c*) dependence of the energy of travelling rolls with $\alpha = 90°$, $Ma = 1300$ (triangles) and stationary longitudinal rolls with $\alpha = 0°$, $Ma = 1300$ (squares); (*d*) Nusselt number for travelling rolls and for stationary rolls (resolution $32 \times 64 \times 32$).

the velocity fields and defined as

$$E = \frac{\dfrac{1}{V_{xyz}} \displaystyle\int \left(v_x^2 + v_y^2 + v_z^2\right) \mathrm{d}x\, \mathrm{d}y\, \mathrm{d}z}{\displaystyle\int U_0(z)^2\, \mathrm{d}z} - 1,$$

here, V_{xyz} is the volume of the computational domain, $U_0(z)$ the velocity profile of the return flow. This quantity characterizes the difference between the kinetic energy of the actual convective flow at the given parameter value and that of the parallel return flow.

To characterize the convective heat transport across the liquid layer, we can introduce the Nusselt number. We use the definition of Thual (1992),

$$\widetilde{Nu} = 1 + Pr^2 Nu,$$

where Nu is actually the convective correction to the total Nusselt number,

$$Nu = \langle v_z \theta \rangle^{xyz}.$$

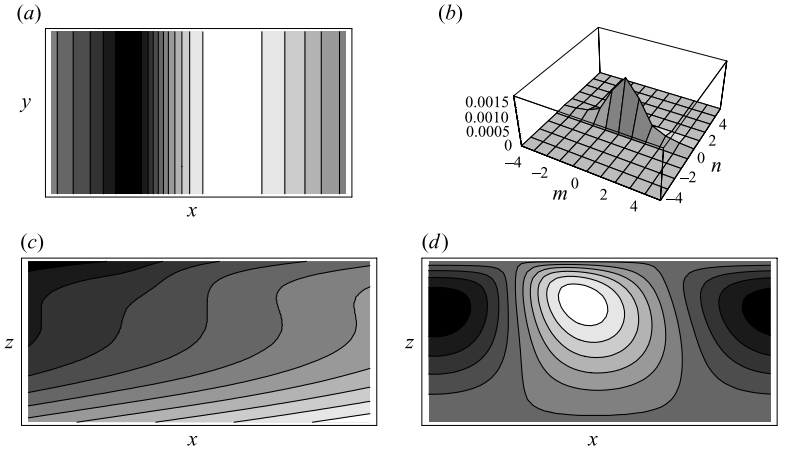

FIGURE 8. The structure of the travelling rolls with $\alpha = 90°$, for parameters $Ma = 1300$ and $A = 0.0205$. (*a*) temperature field $\theta(x, y, 1)$ in the plane x, y at $z = 1$; (*b*) Fourier spectrum; (*c*) isotherms $T(x, 0, z)$ in the plane x, z at $y = 0$; (*d*) isolines of the stream function $\psi(x, 0, z)$.

Here,

$$\langle f \rangle^{xyz} = \frac{1}{L_x L_y} \int_0^{Lx} \int_0^{Ly} \int_0^1 f \, \mathrm{d}x \, \mathrm{d}y \, \mathrm{d}z.$$

All the amplitude curves start with zero values of amplitudes at corresponding instability boundaries. The squares in figure 7(*a*, *b*) present the stationary rolls with $\alpha = 0°$, at Marangoni number $Ma = 850$ in the computation domain with $k_x = 3.2$ and $k_y = 5$ under different values of the temperature gradient. Figure 7(*a*) shows the change in the kinetic energy of the fluid motion, figure 7(*b*) represents the change in the heat transfer across the liquid layer with the change of the horizontal temperature gradient A.

The integral characteristics for the travelling rolls ($\alpha = 90°$) drifting down the main flow are presented in figure 7(*c*, *d*), (triangles). Also, these figures include the properties of the longitudinal rolls with $\alpha = 0°$ (squares). Calculations have been made for $Ma = 1300$, and for the computational domain having horizontal size $L_x = 2.12$ ($k_x = 2.96$) and $L_y = 1.05$ ($k_y = 6$). Simulations were started from the point ($Ma = 1300$, $A = 0.022$) located on the instability boundary for rolls with $\alpha = 90°$ and extended in the direction of decreasing temperature gradient values.

At point C, the travelling rolls (triangles) lose their stability and stationary rolls with $\alpha = 0°$ appear (squares). In figure 7(*c*), we can see that for values of A less then A_C, stationary rolls have higher energy than that of drifting rolls. When increasing the temperature gradient A, the back transition to the longitudinal rolls occurs at point B when stationary rolls disappear. Also, it can be seen that there is a range of temperature gradient values $A_C < A < A_B$ where, depending on the initial state, two numerically stable regimes are reached. We cannot exclude the possibility that one of the regimes is actually metastable, and a transition to another regime takes place after a long time period. Generally, the stationary longitudinal rolls with $\alpha = 0°$ provide better heat transfer across the liquid layer than travelling rolls with $\alpha = 90°$ in the broad range of the values of temperature gradient less then $A < 0.021$.

The structure of the drifting rolls with $\alpha = 90°$ is plotted in figure 8 for the fixed time moment. This result is obtained for $Ma = 1300$ and $A = 0.0205$. Figure 8(*a*)

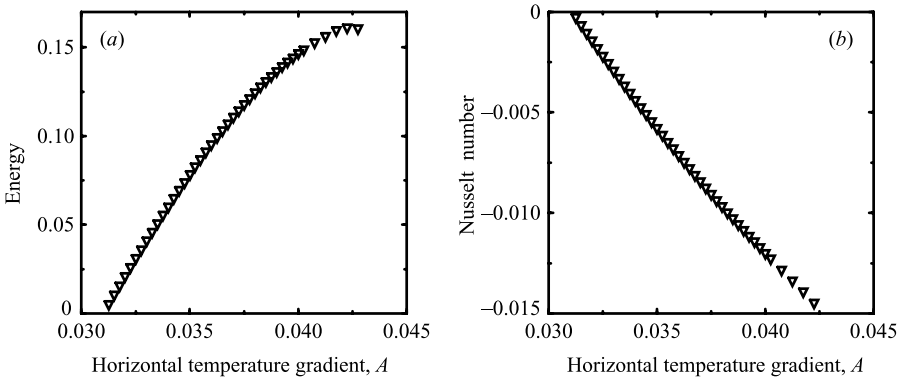

FIGURE 9. The bifurcation diagrams for the oblique hydrothermal waves. (*a*) Dependence of the energy on gradient A; (*b*) dependence of the Nusselt number on gradient A. The spatial resolution $64 \times 64 \times 32$.

demonstrates isotherms of the temperature deviation $\theta(x, y, 1)$ on the surface of the layer. They have the form of lines which are parallel to the y-axis and move from right to left in the direction of the main flow.

To investigate the structure of the flows, later on we use the Fourier spectra of the field $\theta(x, y, 1)$. Figure 8(*b*) presents the Fourier spectra of the roll pattern with $\alpha = 90°$. The vertical axis demonstrates the absolute values $|\widehat{\widehat{\theta}}^{(m,n)}|$ of harmonics included in the series

$$\theta(x, y, z = 1) = \sum_{m=-N_x/2}^{N_x/2-1} \sum_{n=-N_y/2}^{N_y/2-1} \widehat{\widehat{\theta}}^{(m,n)} \exp(\mathrm{i}(mk_x x + nk_y y)).$$

Here, m and n are the harmonics numbers in the x- and y-directions and $k_x = 2\pi/L_x$, $k_y = 2\pi/L_y$. The components with $|m|, |n| \leqslant 5$ only are shown in the Fourier spectra. The central peak $m = 0, n = 0$ presents the average distortion of the interfacial temperature due to the convective flow. Its height is shown schematically because it is much larger than other components.

Figure 8(*c*) demonstrates the total temperature field $T(x, 0, z)$ in the vertical (x, z)-plane. It is distorted mainly by the parabolic profile of the main flow. Isotherms on the left-hand side are darker (colder) then on the right-hand side (lighter and hotter), according to the direction of the applied horizontal temperature gradient. Figure 8(*d*) shows isolines of the stream function $\psi(x, 0, z)$ as a function of x, z (this function can be defined in the plane orthogonal to the roll axis, because the velocity component along the roll axis gives no contribution into the continuity equation).

6.2. *Oblique hydrothermal waves*

Now we turn to another kind of convective regime predicted by the linear theory. The bifurcation diagrams showing the changes of the integral characteristics of the oblique travelling waves moving upstream are presented in figure 9. Calculations have been performed for the section in the parameter plane at Marangoni number $Ma = 1324.6$ and for the computational domain with sizes $L_x = 7.7$ and $L_y = 6.01$. According to the linear theory, in this domain, the waves appear with $\alpha = 38°$. The size of the computational domain was twice as large as necessary for the simulation of this convective pattern. Actually for waves with $\alpha = 38°$, the smallest domain has $L_x = 3.85$ ($L_x = 2\pi/(k_c \sin\alpha)$), $L_y = 3$ ($L_y = 2\pi/(k_c \cos\alpha)$) for $k_c = 2.65$. Unlike the case

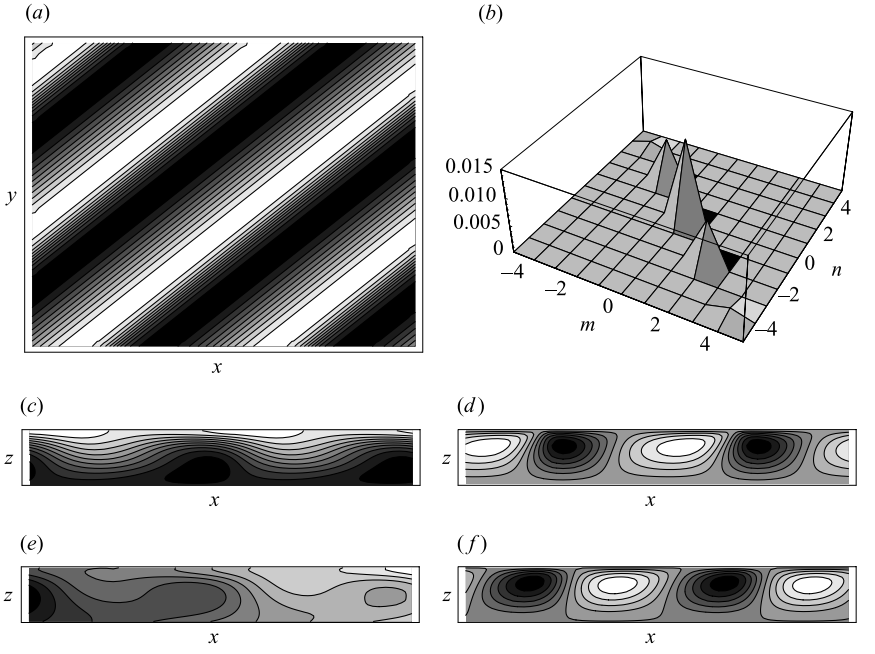

FIGURE 10. The structure of the oblique travelling waves for $\alpha = 38°$, $Ma = 1324.6$ and $A = 0.042$. (*a*) deviation temperature field $\theta(x, y, z = 1)$ on the surface; (*b*) Fourier spectrum; (*c*) deviation temperature field $\theta(x, y = 0, z)$ in the plane x, z; (*d*) the vertical velocity $v_z(x, y = 0, z)$; (*e*) the isotherms $T(x, z, y = 0)$ in the plane x, z; (*f*) stream function $\psi(x, y = 0, z)$.

of the rolls moving down the main flow (previous section), the energy of the hydrothermal waves grows with increasing horizontal temperature gradient (figure 9*a*). Moreover, the dependence of the Nusselt number on the horizontal temperature gradient (figure 9*b*) looks quite unusual: the convective correction to the Nusselt number caused by the appearance of hydrothermal waves is negative, $Nu < 0$.

Because hydrothermal waves move upstream, they rearrange the temperature field in the bulk of the fluid layer in a special way. The typical structure of the travelling waves is shown in figure 10. The isotherms of the temperature deviation $\theta(x, y, 1)$ on the layer surface are shown in figure 10(*a*). The Fourier spectrum is given in figure 10(*b*). In order to explain the above-mentioned unusual property of the hydrothermal waves, let us consider the field of the temperature deviation $\theta(x, 0, z)$ (figure 10*c*) and the field of the vertical velocity $v_z(x, 0, z)$ in the plane $y = 0$ (figure 10*d*). Because of the roll structure of the pattern, the distributions of θ and v_z in any plane $y = \text{const}$ are similar. We can see that the maxima and minima of θ on the surface (at $z = 1$) are located approximately above the corresponding maxima and minima of v_z, i.e. the surface temperature is relatively high where the fluid moves upwards, and it is relatively cold where the fluid moves downward. However, it is characteristic for the hydrothermal waves that the locations of the temperature deviation maxima (which can be found as the lowest points of isotherms) and minima at $z < 1$, are essentially shifted with respect to those at $z = 1$. The phase shift between the distributions of θ and v_z turns out to be more then a quarter of the period everywhere, except a thin region near the surface, which gives a small contribution in $\langle v_z\theta \rangle^{xyz}$, because v_z is small near the interface. That is why the expression for the convective Nusselt number is negative.

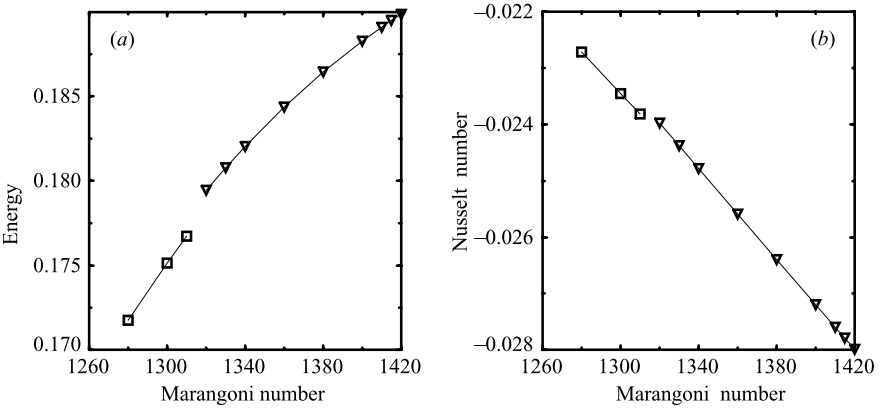

FIGURE 11. Variations of the energy and the Nusselt number for convective regimes obtained at fixed horizontal temperature gradient $A = 0.05$.

The total temperature field $T(x, z, 0)$ is given in figure 10(e). Note that in a large part of the computational domain, the vertical component of the temperature gradient is directed upwards (unlike the case shown in figure 8c). This is essential for the excitation of hydrothermal waves (see Davis 1987). Because the pattern is two-dimensional, we can define the streamfunction for it in the usual way (figure 10f). The intensities of the 'light vortices' (where the rotation is counterclockwise) are slightly larger than those of 'dark vortices' (where the rotation is clockwise). Indeed, for the 'light vortices', the direction of the liquid motion at the surface coincides with the direction of the surface-tension gradient. Therefore, this kind of vortex is supported by the mean temperature gradient. The locations where the liquid has the maximum vertical velocity can be seen in figure 10(d) as the centres of the light spots of the velocity field.

Summarizing the results of this and previous sections, let us mark the distinctive behaviour of the convective patterns near the stability boundary of the return flow. This analysis shows that in the domains of stable roll patterns with $\alpha = 0^\circ$ and $\alpha = 90^\circ$, in spite of the temperature gradient A increasing and bringing energy to the system, the amplitude of the convective component of the fluid motion decay up to zero on the instability boundary (figure 7). On the opposite side of the stability domain, the convective component of the fluid motion begins to rise again with increasing A (figure 9), from the instability boundary of the hydrothermal waves. The excitation of all the instability modes is supercritical.

Also, we carried out the computation for the fixed value of the horizontal temperature gradient $A = 0.05$, and for changing Marangoni number. Results are presented in figure 11. Simulations have been performed in the computational domain with $L_x = 7.7$ and $L_y = 6.01$. It turns out that there is a certain region of parameters, where the hydrothermal waves are modulated in space and in time. In this parameter region, we have observed a new type of pattern, the *oscillating flow*, which is denoted by squares in figure 11. Unlike the previous case of pure hydrothermal waves, the Nusselt number and the energy change with time. The squares show the mean value of the integral characteristics after averaging over the time period T. The periodic oscillations of the integral characteristics are almost sinusoidal. The surface temperature fields for the main four phases of these oscillations corresponding to time instance $T/4$, $T/2$, $3T/4$, T are shown in figures 12(a)–12(d) ($Ma = 1310$, $A = 0.05$).

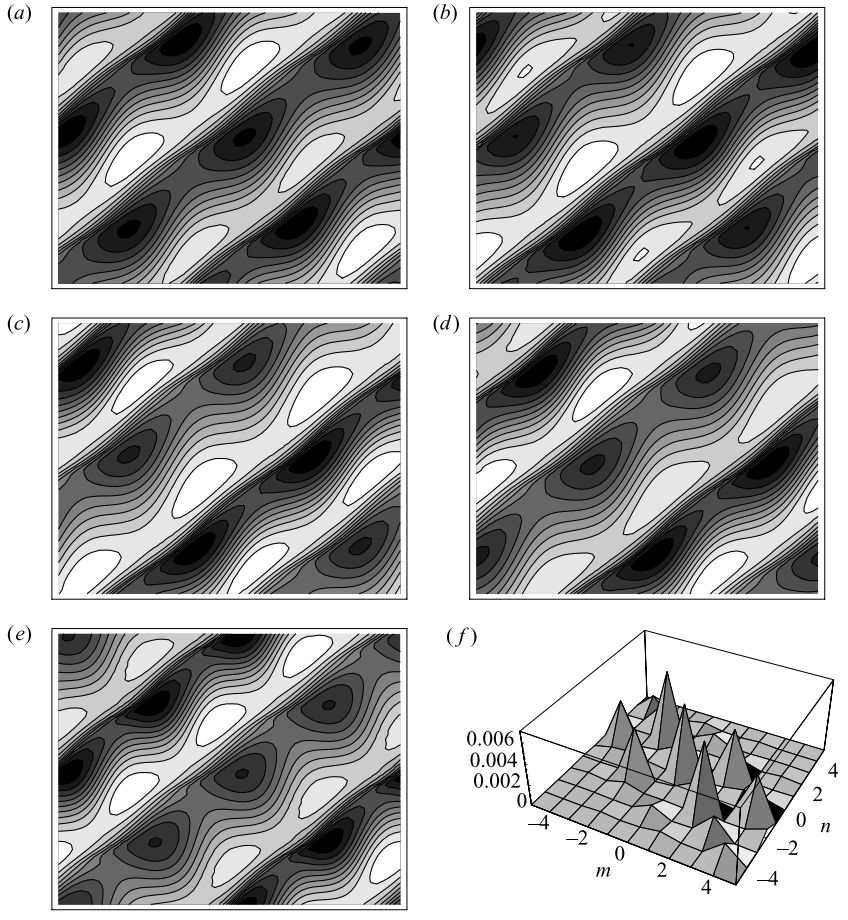

FIGURE 12. Structures of phases of the oscillating flow at $Ma = 1310$, $A = 0.05$. (*a*) $T/4$; (*b*) $T/2$; (*c*) $3T/4$; (*d*) T; (*e*) isotherms $\theta(x, y, z = 1)$ of the stationary regime at $Ma = 1420$, $A = 0.05$; (*f*) Fourier spectrum.

With the increase of the Marangoni number, this flow turns into the stable regime of spatially modulated travelling hydrothermal waves which are shown by triangles in figure 11. The structure of this regime obtained at $Ma = 1420$, $A = 0.05$ is shown in figure 12(*e*, *f*).

6.3. *Hexagonal cells versus rolls*

In this section, we determine the existence domains for the rolls predicted by the linear theory and for hexagonal cells which we expect should arise as well. We are interested in how hexagonal cells and rolls share the parameter plane (Ma, A). Also, we are going to explore the transition between these structures.

For this purpose, we construct the computation domain suitable for both rolls and hexagonal cells. The size of the computation domain is determined by the critical wavenumber found in the linear theory for the rolls ordered along the flow ($\alpha = 0$). So, we fix the aspect ratio along the y-axis as $l_y = 4\pi/k_c$. In order to allow the existence of the hexagonal cells, we can choose the aspect ratio along the x-axis as $l_x = 4\pi/\sqrt{3}k_c$. For reasons which we explain later, we carry out the calculation with the aspect ratio $L_x = 2l_x$ and $L_y = l_y$.

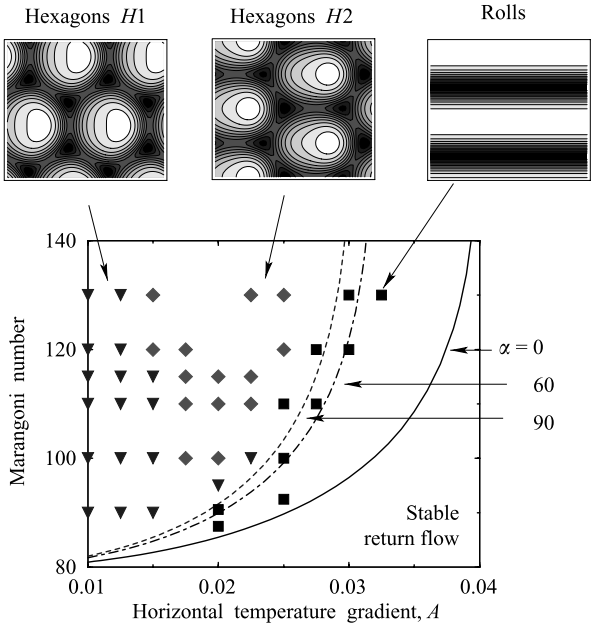

FIGURE 13. Different structures arising from the initial state with 'equal' amplitudes. Isotherms on the surface of the layer are shown above the graph. Spatial resolution $64 \times 64 \times 16$ has been used.

The results of these simulations are shown in figure 13. It turns out that for a relatively small Marangoni number, different patterns arise in the corresponding domains of the parameter plane (Ma, A). The region of roll existence is adjoint to the corresponding instability boundary for rolls with $\alpha = 0°$. All the roll-like disturbances within the range $0° < \alpha < 90°$ start to grow in the domain between the lines $\alpha = 0°$ and $\alpha = 90°$. Thus, the modes which are necessary for forming a hexagonal cell become unstable to the left of the boundary where the rolls appear. Therefore, the region of hexagon existence is located to the left of the region occupied by rolls in figure 13, i.e. in the direction of decreasing horizontal temperature gradient.

Depending on the initial state, two kinds of hexagonal cell appear which are differently aligned with respect to the main flow. For the sake of convenience later on, we call them $H1$ and $H2$ (see figure 13). Typically, we have chosen the initial state with equal amplitudes of all Fourier harmonics, $\widehat{\theta}^{(p,m,n)}(t=0) = 0.1$ in (18) as the initial values. Such a choice provides the 'equal opportunities' for the future evolution of each of them. At the top of the figure, the isotherms on the surface of the layer for different patterns are presented. The light spots show high-temperature regions where the fluid goes up, whereas the dark ones present the low-temperature regions where the fluid sinks. Hexagonal cells $H2$ are deformed because calculations are carried out in the domain with the ratio of sizes appropriate for hexagons of the first kind, $H1$. The intention to obtain both kinds of hexagon is the reason we chose to double the size of the calculation domain. It is the smallest domain where both kinds of the hexagon can be obtained.

In order to obtain non-deformed hexagons, we have used different sizes of calculation domains. In figure 14, the structures of these two kinds of hexagonal cell, $H1$ and $H2$, are shown in more detail. In the former case, the size of the cell is $L_x = 2l_x$, $L_y = l_y$, in the latter case $L_x = l_x$, $L_y = 2l_y$. Each structure is represented by the superposition

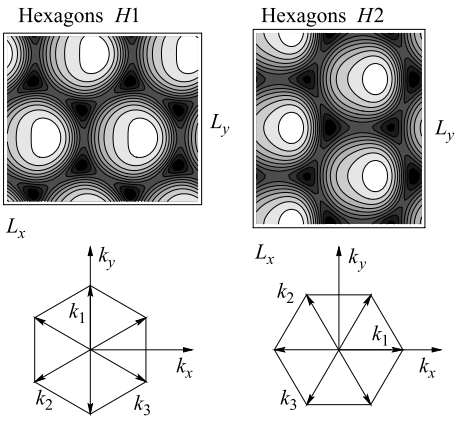

FIGURE 14. The upper diagrams show the structure of the hexagonal cells ordered along and across the main flow. The basic return flow on the surface is directed to the left. The lower diagrams show superpositions of the wavevectors which form the hexagonal cells.

H_1	H_2
$\boldsymbol{k}_1 = k_c \boldsymbol{e}_y$	$\boldsymbol{k}_1 = k_c \boldsymbol{e}_x$
$\boldsymbol{k}_2 = k_c\left(-\frac{1}{2}\sqrt{3}\,\boldsymbol{e}_x - \frac{1}{2}\boldsymbol{e}_y\right)$	$\boldsymbol{k}_2 = k_c\left(\frac{1}{2}\sqrt{3}\,\boldsymbol{e}_y - \frac{1}{2}\boldsymbol{e}_x\right)$
$\boldsymbol{k}_3 = k_c\left(\frac{1}{2}\sqrt{3}\,\boldsymbol{e}_x - \frac{1}{2}\boldsymbol{e}_y\right)$	$\boldsymbol{k}_3 = k_c\left(-\frac{1}{2}\sqrt{3}\,\boldsymbol{e}_y - \frac{1}{2}\boldsymbol{e}_x\right)$
$l_x = 4\pi/\sqrt{3}k_c,\ l_y = 4\pi/k_c$	$l_x = 4\pi/k_c,\ l_y = 4\pi/\sqrt{3}k_c$

TABLE 1. Geometrical parameters of two kinds of hexagon.

of three rolls with wavevectors $\boldsymbol{k}_1$, $\boldsymbol{k}_2$, $\boldsymbol{k}_3$ (see table 1) such that the angles between each two wavevectors are equal to 120°:

$$\theta(\boldsymbol{x}, z) = f(z) Re\left[\sum_{j=1}^{3} \exp(\mathrm{i}\boldsymbol{k}_j \cdot \boldsymbol{x})\right].$$

These two kinds of pattern correspond to two different orientations of the hexagonal cell with respect to the direction of the main flow. Wavenumber k_c for cells $H1$ and $H2$ has been chosen according to the linear theory for the rolls with $\alpha = 0°$ and $\alpha = 90°$, respectively.

6.4. *Transitions between patterns*

The fact that in our previous calculation (§ 6.3) in the computation domain suitable for $H1$, hexagons $H2$ arise also and are located closer to the instability boundary (figure 13) gives some reason to consider the evolution of these two kinds of hexagon separately. We are also interested in considering other regimes which could survive in these domains at different values of control parameters (Ma, A).

It is known that in the absence of the horizontal temperature gradient $A = 0$, the square patterns replace the hexagonal cells when the Marangoni number increases. This was demonstrated numerically by Bestehorn (1996) and confirmed experimentally by Nitschke & Thess (1995).

We fix the 'double' aspect ratio as was done for hexagons formerly (figure 14). The double size provides a wider variety of the regimes permitted in the domain (in

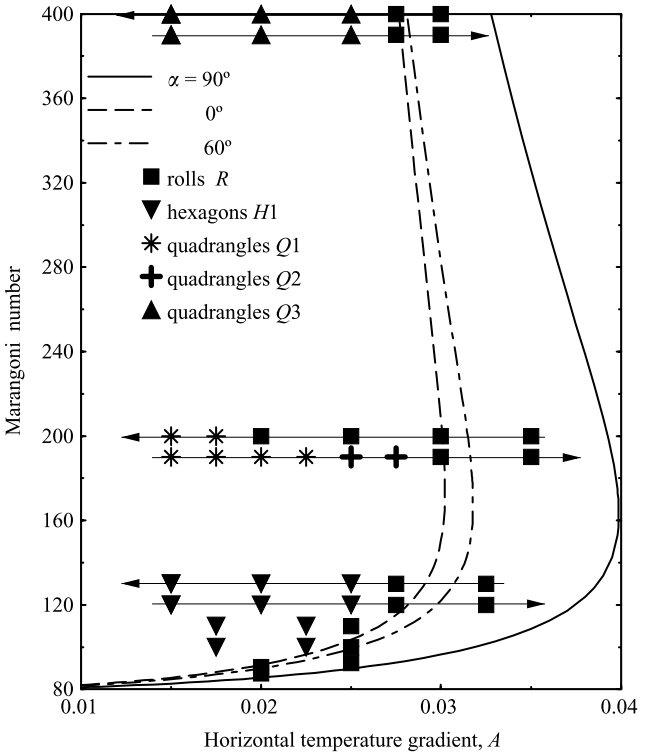

FIGURE 15. The diagram of the transitions between patterns which occur with the temperature gradient changing. Calculations have been performed in the computational domain suitable for hexagons $H1$. Arrows show the direction of the temperature gradient changing. Solid, dashed and dot-dashed lines are the instability boundaries for rolls with different angles α.

comparison with the domain occupied by a single hexagon only). Figures 15–17 show two series of calculations which have been performed in the double computation domains suitable for $H1$ and $H2$.

First, consider the evolution of the convective flows in the computation domain suitable for $H1$ by changing the horizontal temperature gradient (figure 15). The computation domain was constructed using the critical wavenumber k_c given by the linear theory for the curve $\alpha = 0^\circ$ at the corresponding Marangoni number (as was described in the previous section). We have carried out three series of simulations fixing Marangoni number (sections at $Ma = 120$, 200, 400) and changing the temperature gradient only. In all these cases, we started from roll patterns with $\alpha = 0^\circ$ near the boundary of their stability and moved in the direction of decreasing horizontal temperature gradient A (arrows to the left). During this process, every new regime was used further as an initial state for the next convective structure. When we had achieved the point of zero temperature gradient $A = 0$, we 'turned back' and started to monitor the flow evolution under increasing horizontal temperature gradient (arrows to the right). Eventually, we came back to the roll patterns again. Note that the calculations with increasing and decreasing values of A have been done for the same value of the Marangoni number. The forward and back sequences of the regimes are different and therefore, for convenience, we have shown them on figure 15 on different lines. The location of the forward transition point from rolls to a three-dimensional cellular pattern generally does not coincide with the point of the inverse

transition from a three-dimensional pattern to rolls. Different signs in figure 15 stand for different convective flows. Black squares stand for rolls. The extreme left-hand square demonstrates the leftmost point of the rolls domain where they are still stable. Triangles (down) stand for hexagonal cells $H1$ and every extreme right-hand triangle shows the rightmost point where hexagonal patterns were obtained. Also, the instability boundaries for rolls with angle α equal to 0°, 60° and 90° are shown in figure 15. So we can see that for relatively small values of the Marangoni number, the transition areas from longitudinal rolls R to hexagons $H1$ and back are located not far from the instability boundary for rolls $\alpha = 60°$, which form the hexagonal pattern. To the right of this boundary and up to the instability boundary, there are longitudinal rolls with $\alpha = 0°$ only.

Note that the critical wavenumbers for longitudinal rolls with $\alpha = 0°$, at section $Ma = 120$, 200, 400 are $k_c = 2.15$, 2.4, 3.1, respectively. Thus, the area of the computational domain, constructed on these wavenumbers, $S_{xy} = L_x L_y = 32\pi^2/(\sqrt{3}k_c^2)$ decreases (39.4, 31.7, 19, respectively) with the increase of the Marangoni number.

During the calculations in these domains, besides hexagonal and roll cells, three different kinds of quadrangle cell have been obtained (figure 18). Pattern $Q1$ (stars in figure 15) contains four cells in the computation domain. Pattern $Q2$ (crosses in figure 15) contains two cells, and pattern $Q3$ (triangles with vertices upward in figure 15) contains only one cell. We can see that patterns $Q1$ and $Q2$ are observed at equal Marangoni number but different values of the horizontal temperature gradient A. Pattern $Q3$ exists at sufficiently larger Marangoni numbers. We can see that for horizontal temperature gradient values $A < 0.02$, the quadrangle cell $Q1$ at $Ma = 200$ has an area of about $31.7/4 = 7.9$, whereas the cell $Q3$ at $Ma = 400$ has an area of about 19 dimensionless units, that is larger then the previous one for $Q1$. It is remarkable that the boundaries of the cells $Q1$ and $Q3$ are ordered parallel to the sides of the computational domain ('rectangles'), unlike pattern $Q2$ which has inclined cells boundaries ('rhombi').

All the patterns described above move from the right to the left in the direction of the surface-tension gradient.

In order to consider the transition between longitudinal rolls with $\alpha = 0°$ and hexagons $H1$ in more detail, we have carried out a simulation at a fixed Marangoni number, $Ma = 115$, changing horizontal temperature gradient A only. The results are shown in figure 16. The vertical axis presents the kinetic energy of the fluid motion,

$$E_k = \frac{1}{2V_{xyz}} \int \left(v_x^2 + v_y^2 + v_z^2\right) \mathrm{d}x\, \mathrm{d}y\, \mathrm{d}z.$$

We have observed gradual changes of the structure from a hexagonal pattern toward a roll pattern with gradient A increasing. The black squares stand for the pure roll patterns. Triangles stand for the transition patterns containing closed isolines. We should note that for the range of $0.023 < A < 0.025$, for each temperature gradient value there are two branches of solutions. The bottom branch presenting pure rolls is unstable, i.e. it can be destroyed by an arbitrary little perturbation having hexagonal components, and finally the solution comes to the upper hexagonal branch. This transition scenario agrees with the result of the weakly nonlinear analysis presented in § 4 (see also Malomed *et al.* 1994).

The results of calculations that were carried out in the computational domain suitable for hexagons $H2$ is presented in figure 17. The wavenumber which is needed for constructing this computational domain is taken equal to the critical wavenumber on the instability boundary for the rolls with $\alpha = 90°$ which take part

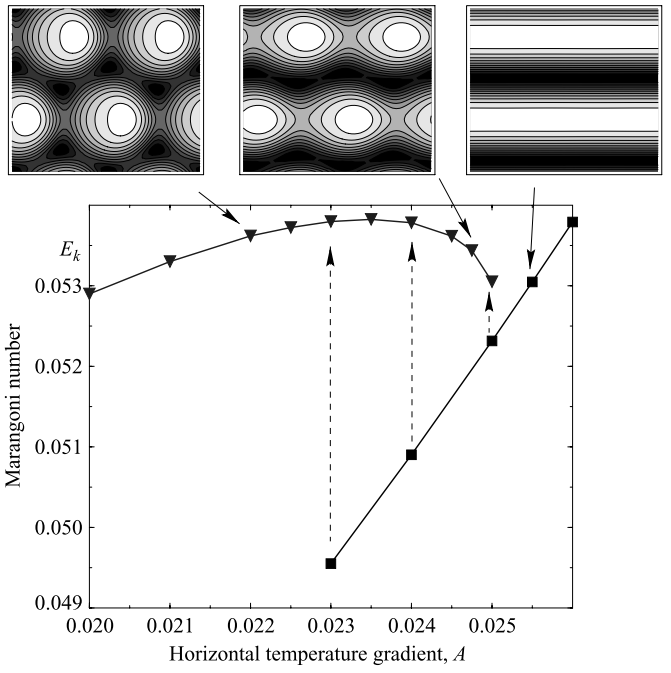

FIGURE 16. The transition between hexagons $H1$ and rolls which occur with the temperature gradient changing ($Ma = 115$).

in forming hexagonal pattern $H2$. In this case, we have also done three series of simulations corresponding to three different values of the Marangoni number (sections at $Ma = 130$, 200, 400). Similarly to the previous case, figure 17 shows the transitions between different patterns, which take place under the temperature gradient A decreasing and then increasing. We can see again that the forward transition taking place at $Ma = 130$ from the rolls with $\alpha = 0^\circ$ (squares in figure 17) to the hexagons $H2$ (rhombi in figure 17) under temperature gradient decreasing and back transition with the temperature gradient increasing occur in different ways. At the forward transition, we observe that longitudinal stationary rolls with $\alpha = 0^\circ$ turn into hexagonal patterns near the instability boundary for rolls with $\alpha = 60^\circ$ (dot-dashed line). Under the back transition, first, hexagons $H2$ turn into oblique drifting rolls with $\alpha \simeq 30^\circ$ (dots in figure 17) and then they turn into longitudinal rolls with $\alpha = 0^\circ$. So, there is a hysteresis domain between the rolls with $\alpha = 0^\circ$ and hexagons $H2$.

Thus, with the growth of the temperature gradient A, we observed the transition from moving hexagonal patterns to longitudinal rolls and then to the parallel return flow.

The next series of calculations has been carried out at $Ma = 200$. Under decreasing temperature gradient A, the rolls with $\alpha = 0^\circ$ turn into the quadrangles $Q2$ approximately at the instability boundary for rolls with $\alpha = 60^\circ$ (forward transition). Then, quadrangle cells $Q2$ turn into cells $Q1$. This flow maintains that configuration until gradient A disappears. Under the back transition, quadrangle cells $Q1$ turn into hexagons $H2$ which then turn into oblique drifting rolls with $\alpha \simeq 30^\circ$ and eventually they again become stationary longitudinal rolls with $\alpha = 0^\circ$.

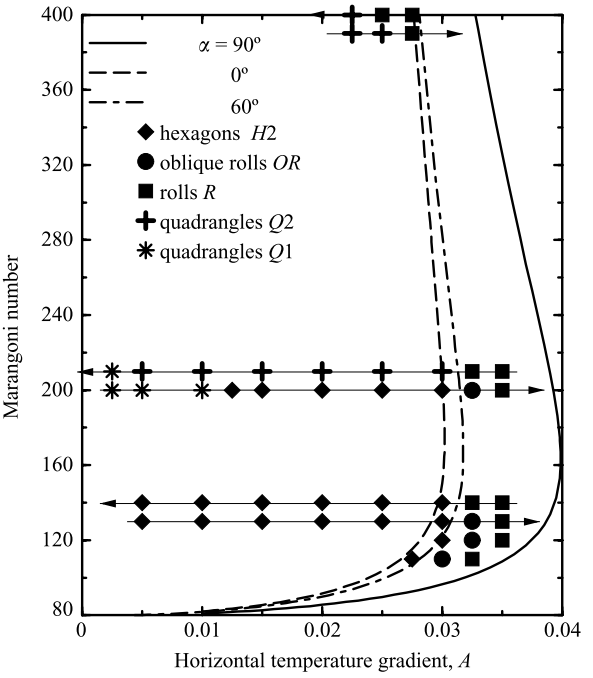

FIGURE 17. The diagram of the transitions between patterns which occur with the temperature gradient changing. Calculations have been performed in the computational domain suitable for hexagons $H2$. Arrows show the direction of the temperature gradient changing. Solid, dashed and dot-dashed lines are the instability boundaries for rolls with different angles α.

At $Ma = 400$, we have obtained only a transition between longitudinal rolls with $\alpha = 0^\circ$ and quadrangle cells $Q2$. We have observed the quadrangle $Q2$ until gradient A disappears.

During the calculations in this domain, we have obtained the same set of patterns as in the first case except for quadrangle pattern $Q3$ and the additional roll pattern with $\alpha = 30^\circ$, which takes part in forming hexagons $H2$. Perhaps this is beacuse pattern $Q3$ requires a rectangle computational domain with the x-boundary side longer then the y-boundary side. In the case of the second computational domain it is not so.

Figures 18 and 19 show the structures of the convective flows which have been obtained in simulations presented in figures 15 and 17. They show isotherms $\theta(x, y, 1)$ on the surface of the layer for different convective patterns. All convective structures are distorted by the main return flow.

Note that we cannot be sure that structures presented in the last two figures include all the patterns which are possible in this parameter domain. All these patterns have been obtained using particular initial conditions. In both series of experiments, we started from longitudinal rolls with $\alpha = 0^\circ$. Most probably that it is only one possible scenario of the transitions between patterns. All described patterns move to the left according to the direction of the main flow.

As a result of these two series of calculations presented in figures 15 and 17, we can see that the regions of stability of the hexagonal patterns are located at a lower Marangoni number than those of the quadrangle patterns. Under increasing Marangoni number and a fixed value of the horizontal temperature gradient A, hexagonal patterns turn into quadrangles. Qualitatively, this result is in accordance

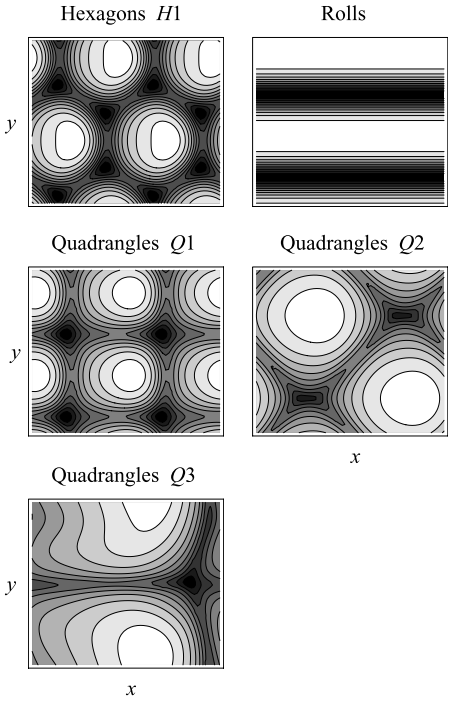

FIGURE 18. Convective patterns obtained in the calculation domain suitable for hexagons $H1$, and their Fourier spectra.

with the result of Bestehorn (1996) that in the absence of the temperature gradient A, the domain where the quadrangles (squares) are stable is located above the stability domain of the hexagonal patterns.

6.5. *Simulations with the large aspect ratio*

All the simulations in the previous sections were performed in computational domains of size commensurable with the convective structures, i.e. they contained only a few cells. In order to consider the influence of the temperature gradient on the possible mutual coexistence of different regimes and to check our previous results, we have carried out simulations in a large domain $L_x = L_y = 20$ using the spatial resolution $128^2 \times 16$. Here we list the possible patterns, compatible with the geometry of the domain and boundary conditions. The set of the convective regimes which have been observed for different parameters values is shown in figures 20–22.

In the absence of the horizontal temperature gradient ($A = 0$), the appearing hexagonal patterns have a slightly non-equilateral form. Hexagons turn out to be ordered along the axis having a slope with respect to the boundaries of the computational domain. It is the result of the square shape of the computational domain, $L_x = L_y$. A perfect hexagonal pattern can be obtained in the domain with non-equilateral sides (as it was done in § 6.3). In the presence of a little horizontal temperature gradient, this convective structure does not change. The pattern of this type is presented in figure 20*a* ($Ma = 200$, $A = 0.01$). This kind of hexagonal pattern can be considered as slightly oblique hexagons $H1$. Later on we call them OH_+. Computation carried out for parameters $Ma = 150$, $A = 0.02$, using other initial conditions, led to oblique hexagonal patterns with the opposite slope with respect to the x-axis corresponding to the direction of the horizontal temperature gradient

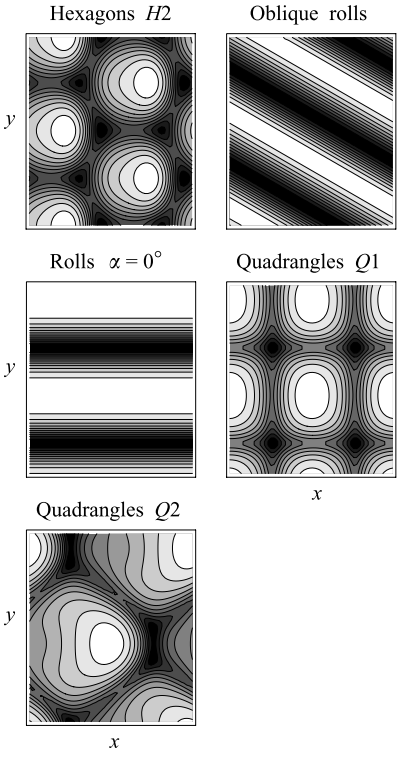

FIGURE 19. Convective patterns obtained in the calculation domain suitable for hexagons $H2$, and their Fourier spectra.

($A \cdot \boldsymbol{e}_x$). It is the pattern in figure 20(a) reflected with respect to the x-axis (we call them OH_-). An example of non-oblique hexagonal patterns $H1$ was obtained for larger horizontal gradient values $Ma = 140$, $A = 0.025$ (figure 20b). Owing to the action of the relatively stronger horizontal temperature gradient, hexagons are ordered along the x-axis. Under temperature gradient A growing further, they turn into stationary longitudinal rolls with $\alpha = 0$ (as was described in § 6.4, figure 16).

The next convective structure that we consider is the pure hexagonal pattern $H2$ (figure 20c), which has been obtained for parameters $Ma = 140$, $A = 0.027$. The region where this pattern can be obtained (if we start from the initial date with 'equal' amplitudes as was described in § 6.3) is located at the relatively larger values of the horizontal temperature gradient than the analogous region of $H1$. Recall that the transverse rolls with $\alpha = 90°$ take part in forming hexagonal pattern $H2$, whereas longitudinal rolls $\alpha = 0°$ form pattern $H1$. Therefore, in the structure $H2$, the convective cells are ordered parallel to the y-axis, unlike structure $H1$.

For some values of Ma (often coinciding with the area of the appearance of $H2$), we have observed irregular patterns, a typical example of which is presented in figure 20(d). This snapshot of a non-stationary process is obtained at parameters $Ma = 150$, $A = 0.0265$. We can see shapeless cells which experience oscillation of their form. Some of the cells merge and split. At other parameter values, we can find structures with more visible organization of the cells along the y-axis (that is intrinsic for the structure $H2$), but also with irregular time behaviour of the cells. The example for parameters $Ma = 200$, $A = 0.028$ is shown in figure 21(a). Owing to the apparently chaotic oscillations of the shape of some convective cells, the whole pattern is chaotic

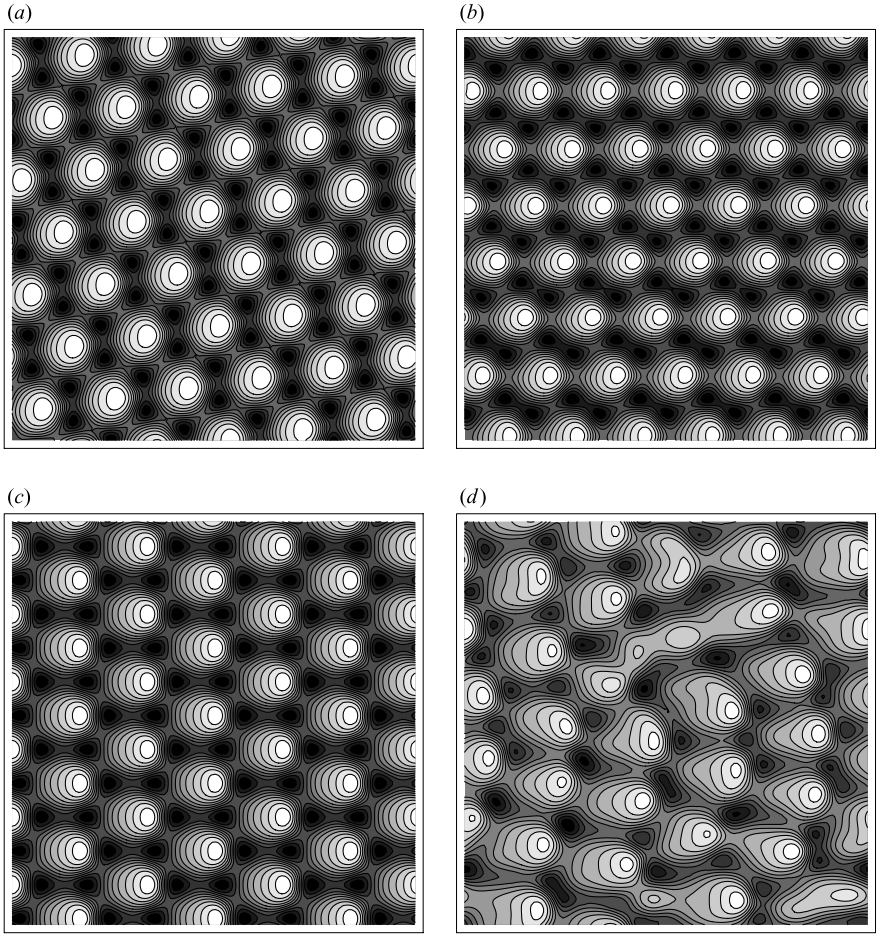

FIGURE 20. Isotherms of various patterns with $L_x = L_y = 20$. (*a*) Structure OH_+ ($Ma = 200$, $A = 0.01$); (*b*) structure $H1$ ($Ma = 140$, $A = 0.025$); (*c*) structure $H2$ ($Ma = 140$, $A = 0.027$); (*d*) structure obtained at $Ma = 150$, $A = 0.0265$.

as well. The integral characteristics like the energy and the Nusselt number of these patterns also experience chaotic oscillations.

The area of stable rolls is situated to the right of the region of stable hexagons $H2$ and the unstable irregular patterns. Depending on parameters (Ma, A) and initial conditions, we have observed roll patterns having different slope α with respect to the x-direction. In accordance with the results of § 6.4 (figures 15, 17), the longitudinal stationary rolls with $\alpha = 0^\circ$ are located near the boundary of the return flow stability. Between the areas of the existence of the hexagonal patterns and the longitudinal rolls, there is a stability domain of the oblique rolls shown in figure 21(*b*). They are inclined to the x-direction on the angle which is just the same as for hexagonal patterns in figure 20(*a*), which has been used as the initial state. We have to recall that in the previous section we have also obtained oblique rolls, but they have another inclination angle (figure 19). This difference is caused by the difference in the size and in the geometry of the computational domains.

Using hexagons $H2$ as the initial state and increasing temperature gradient A, we have obtained the structure shown in figure 21(*c*), half of which is presented by the

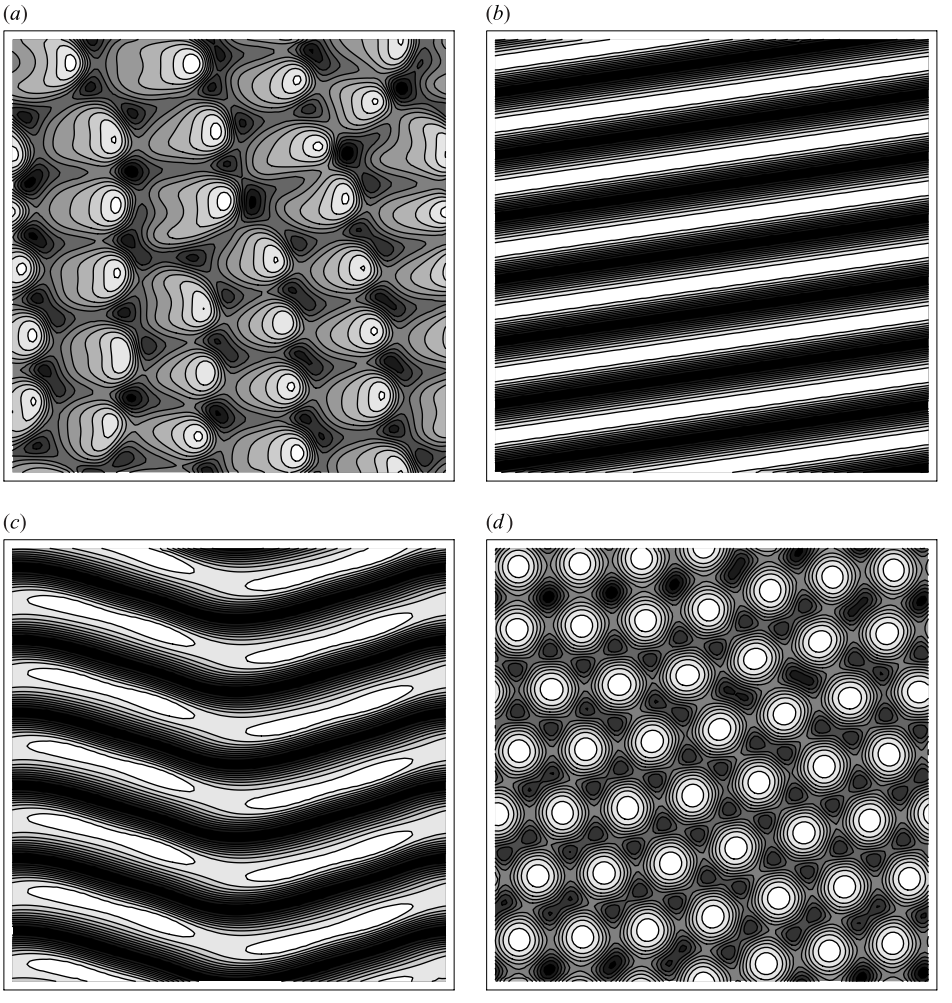

FIGURE 21. Isotherms of various patterns with $L_x = L_y = 20$. (*a*) $Ma = 200$, $A = 0.028$; (*b*) $Ma = 150$, $A = 0.0285$; (*c*) $Ma = 140$, $A = 0.032$; (*d*) $Ma = 200$, $A = 0.001$.

oblique rolls with positive inclination angle and the half consists of rolls with negative inclination angle of the same modulus. This convective pattern can be considered as a system of inclined roll domains separated by domain walls. This pattern has been obtained for the values of parameters $Ma = 140$, $A = 0.032$ where in the computational domain suitable for hexagons $H2$ we had oblique rolls (see figure 17).

The regions of stability of the hexagons $H1$, $H2$ and oblique rolls are compatible with the results obtained in § 6.4 for the computational domains with small aspect ratio (figures 15 and 17). In accordance with these results (figure 17), the oblique rolls stability domain is contained between stability domains for hexagons and longitudinal rolls. However, in the case of a large aspect ratio, the rolls have a smaller inclination angle α. To the right of the region of oblique rolls (in the direction of increasing horizontal temperature gradient values), there is the stability domain of stationary longitudinal rolls with $\alpha = 0^\circ$ which adjoin the boundary of the return flow instability.

It is known that in the absence of the horizontal temperature gradient A, there are convective structures containing some defects or domains of different patterns. An

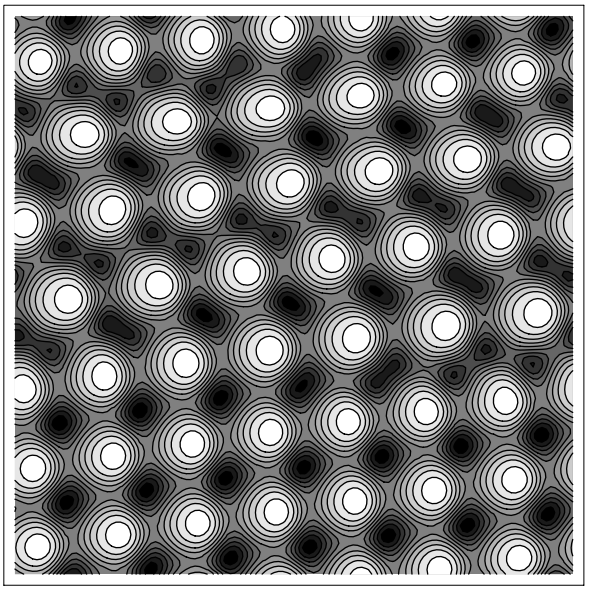

FIGURE 22. Isotherms of the pattern containing quadrangle and hexagonal structures with $L_x = L_y = 20$. $Ma = 220$, $A = 0.01$.

example of such a structure presenting coexisting hexagonal pattern and quadrangles is shown in figure 21(d). In the presence of a moderate temperature gradient A, the situation remains unchanged (figure 22) and we can still observe the structure of mixed hexagonal and quadrangle cells. However, on further increasing gradient A, this structure is destroyed, and it is replaced with an inclined hexagonal pattern similar to figure 20(a).

Note that the stability domains of the different regimes described above can overlap each other and there are parameter values permitting multistable states. It must also be noted that calculations (also as in the results of § 6.4) have shown that the stability domain of the hexagonal patterns is separated from the domain of stable return flow by the strip of stable roll patterns. The existence of this rolls strip is the result of the anisotropy of the problem under consideration, owing to the action of the horizontal temperature gradient. Recall that there is no such rolls strip for the pure problem without horizontal gradient $A = 0$ and the hexagonal patterns bifurcate subcritically from the stability boundary.

In conclusion, we consider the phase velocity of the different hexagonal patterns mentioned above. It is interesting to find out how the convective patterns move with respect to the direction of the temperature gradient A. The direction of the phase velocity can give the answer to this question. We suppose that the stationary convective pattern is constructed from the rolls $\sim \exp(\mathrm{i}\boldsymbol{k}_j(\boldsymbol{r}_j - \boldsymbol{v}t))$ moving in the same direction and with the same phase velocity $\boldsymbol{v}$

$$\omega_j = \boldsymbol{k}_j \cdot \boldsymbol{v}.$$

Here, j is the number of rolls constructing the pattern. In order to determine the direction of the phase velocity $\boldsymbol{v} = (v_x, v_y)$ in the (x, y)-plane it is enough to consider

Planform	v_x	v_y	Nu	E_k
OH_+	−0.186	-8.59×10^{-3}	2.8×10^{-3}	0.116
OH_-	−0.186	8.59×10^{-3}	2.8×10^{-3}	0.116
$H1$	−0.157	0	2.741×10^{-3}	0.115
$H2$	−0.166	0	2.745×10^{-3}	0.115

TABLE 2. Comparison of the phase velocities, Nusselt numbers and energies for four different hexagonal patterns at $Ma = 150$, $A = 0.02$.

only two rolls characterized by (k_x, k_y):

$$k_{1,x} v_x + k_{1,y} v_y = \omega_1,$$
$$k_{2,x} v_x + k_{2,y} v_y = \omega_2.$$

As these two necessary sample rolls, the rolls with maximal values $|\widehat{\theta}^{(j)}| \cdot \exp(\mathrm{i}(k_{j,x}x + k_{j,y}y))$ have been chosen. Then ω_j can be determined by the following relation:

$$\omega_j = -\frac{\tan^{-1}[\mathrm{Im}(\widehat{\theta}^{(j)})/\mathrm{Re}(\widehat{\theta}^{(j)})]^n - \tan^{-1}[\mathrm{Im}(\widehat{\theta}^{(j)})/\mathrm{Re}(\widehat{\theta}^{(j)})]^{n-1}}{\Delta t},$$

where $\Delta t = t^n - t^{n-1}$ is the time step of the numerical procedure.

We should emphasize that the structures OH_+, OH_-, $H1$ and $H2$ are simultaneously stable in a certain region of the parameter plane (Ma, A). For instance, using the patterns shown in figure 20(a, b, c) as the initial condition, we have obtained all the above mentioned structures at the point $Ma = 150$, $A = 0.02$. For comparison of the phase velocity values of different hexagonal patterns, we have chosen this point. As was expected, the convective patterns with little positive OH_+ and negative OH_- inclination angle have the same value x-component of the phase velocity and oppositely directed y-component of the phase velocity. The velocity values are presented in the table 2. The x-component of the phase velocity of the hexagonal patterns $H1$ (figure 20b) and $H2$ (figure 20c) smaller than velocities of the oblique hexagons. Other integral characteristics of these four kinds of hexagonal patterns are almost the same. Note that velocity of the return flow at the surface in this point is $v_{rf} = -0.75$, and it is larger then the phase velocity.

The phase velocity of the domain wall at the point ($Ma = 140$, $A = 0.032$, figure 21c) is $v_x = -0.44$ and $v_y = 0$. For oblique rolls (figure 21b), we can find only the normal component of the phase velocity $v_n = 7.18 \times 10^{-2}$.

7. Conclusion

The results of the investigation make clear the important role of the horizontal temperature gradient on the formation and the development of convective regimes in a plane liquid layer heated from below. For instance, at the fixed relatively small temperature gradient across the liquid layer, ruling only by the longitudinal temperature gradient, we can obtain the hexagonal patterns, the rolls, the parallel return flow, the hydrothermal waves and other different cellular regimes. So we have one more additional parameter for the control of the convective flows.

As a result of the linear stability analysis, three instability modes have been found. It has been found that the transition from the stable parallel return flow to spatially periodic flows occurs through the longitudinal rolls (with the axes directed along the horizontal temperature gradient), drifting rolls moving downstream, or travelling hydrothermal waves moving upstream depending on the control set of parameters. It turned out that in the presence of the inclined temperature gradient, the parallel return flow can be restabilized by the enhancement of the vertical component of the temperature gradient.

Our calculations in the domains with a small aspect ratio revealed the existence of two different kinds of hexagonal patterns ordered along and across the direction of the surface-tension gradient. The latter calculations in the domains with large aspect ratio have confirmed the existence of two hexagonal patterns and have shown that hexagonal patterns with inclined orientation of cells are also possible. Also, it was shown that stationary longitudinal rolls directed along the horizontal temperature gradient provide better heat transfer across the liquid layer than travelling rolls transverse to the horizontal temperature gradient. It should be noted that during all our calculations we have obtained longitudinal rolls more often then transverse travelling rolls. This observation is similar to the result known for buoyancy convection where the longitudinal rolls also are preferred (Kelly 1994).

During the simulations, we have observed different kinds of quadrangle patterns and transitions between them. We have found that the stability region of quadrangle patterns is located above the region of stable hexagonal patterns, as it is in the absence of the horizontal temperature gradient. It turned out that in the presence of the horizontal temperature gradient also there are structures containing defects or domains of different patterns. Specifically, in the large computational domain, we have observed coexisting quadrangle and hexagonal cells and regimes presented by the systems of differently inclined roll domains separated by domain walls.

It is remarkable that the presence of the horizontal temperature gradient shifts the existence domain of the cellular patterns in such a way that the domain of stable return flow states turns out to be surrounded by the various kinds of pure roll patterns and waves predicted by the linear theory. Except for the region near $A = 0$, where there is a direct transition from the return flow to hexagonal patterns, the transition from stable return flow to spatially periodic convective regimes occurs according to the predictions of the linear theory.

When the present paper was in preparation, we learned about the work of Ueno *et al.* (2002) which was the only published experimental work on the thermocapillary convection with an inclined temperature gradient. The direct quantitative comparison of our theoretical predictions with the experimental data is impossible because the experiments are carried out in a cylindrical cavity for silicone oils which have essentially larger values of the Prandtl number. A computation of convective flows in a high-Prandtl liquid filling a closed cavity is beyond the scope of the present paper. Nevertheless, it is remarkable that the same sequence of regimes as that mentioned in § 6.4, namely flowing Bénard cells, nearly longitudinal rolls ('streak convection') and the parallel return flow, have been observed in experiments.

We are grateful to Thomas Boeck for his valuable advice on the preparation of the code treating nonlinear regimes, and to Leonid Braverman who provided us with the code for the calculation of the linear stability boundaries. This work was partially supported by the Minerva Center for Nonlinear Physics of Complex Systems.

Ma	Planform	N_x	N_y	N_z	E_{Boeck}	Nu_{Boeck}	E_{our}	Nu_{our}
80	*HX*	64	32	17	68	0.177	68.13	0.177
82	*HX*	64	32	17	154	0.407	154.39	0.407
86	*HX*	64	32	17	328	0.879	328.27	0.879
88	*DHX*	64	32	17	398	1.03	397.62	1.034
90	*DHX*	64	32	17	440	1.11	439.69	1.110
92	*DHX*	64	32	17	455	1.11	455.12	1.112
95	*R*	64	32	17	467	1.13	466.93	1.130
102	*R*	64	32	17	784	1.87	781.60	1.868
105	*TW*	64	32	17	1110	2.60	1112.5	2.606
110	*TR*	64	32	33	2050	4.71	2049	4.71
115	*TR*	64	32	33	7500	13.8	7586	13.96

TABLE 3. Comparison of the numerical results with no-slip condition at the bottom.

Planform	N_x	N_y	N_z	Nu	E_k	$U(z=1)$
$H1$	16	16	9	2.6851×10^{-3}	0.716740×10^{-1}	−0.3244
$H1$	32	32	9	2.4944×10^{-3}	0.67060×10^{-1}	−0.3246
$H1$	32	32	17	2.4951×10^{-3}	0.67076×10^{-1}	−0.3246
$H1$	65	65	33	2.4951×10^{-3}	0.67076×10^{-1}	−0.3246
$H2$	16	16	9	2.7976×10^{-3}	0.11565	−0.7484
$H2$	32	32	9	2.6141×10^{-3}	0.11066	−0.7487
$H2$	32	32	17	2.6141×10^{-3}	0.11066	−0.7487
$H2$	64	64	33	2.6141×10^{-3}	0.11066	−0.7487

TABLE 4. Comparison of the integral characteristics of the flow for grids having different numbers of the mesh points.

Appendix. Validation of the numerical procedure

For validation of the code simulating the convective regimes we have reproduced the result presented in Boeck (2000, appendix D) for Marangoni convection at a low Prandtl number. This case corresponds to $A=0$, $\langle \partial_x p \rangle = 0$, $\langle \partial_y p \rangle = 0$. The results of the comparison are shown in table 3 for different convective structures. Calculations have been performed for Prandtl number $Pr=0.005$ in the computational domain $L_x = 4\pi/k_c$, $L_y = 4\pi/\sqrt{3}k_c$, where $k_c = 1.9929$.

For definition of the energy of the fluid motion E, see Boeck (2000). The definition of the Nusselt number Nu is given in § 6.1. Here, *HX* stands for hexagonal patterns; *DHX* deformed hexagons; *R* steady rolls; *TW* denotes travelling waves; *TR* travelling rolls (for more detail see Boeck 2000).

In order to check the convergence of the numerical procedure for our problem, we carried out a calculation of the main integral characteristics on a sequence of grids having different numbers of mesh points. Computations were performed for hexagonal pattern $H1$ at the horizontal temperature gradient $A=0.01$, Marangoni number $Ma=130$, and for hexagonal pattern $H2$ at parameters $A=0.02$, $Ma=200$. In the first case, the size of the computational domain was $L_x = 2l_x$, $L_y = l_y$ and $L_x = l_x$, $L_y = 2l_y$ in the second case (parameters l_x, l_y are given in table 1). The time step was fixed at $\Delta t = 0.02$.

Every attempt was started with random initial dates. The Nusselt number, the kinetic energy of the fluid motion and the horizontal velocity on the surface of the liquid layer are shown as a function of the grid mesh points along the x, y, z directions (table 4). The integral characteristics are defined in § 5, 6.1 and 6.4.

REFERENCES

Bestehorn, M. 1996 Square patterns in Bénard–Marangoni convection. *Phys. Rev. Lett.* **76**, 46.

Birikh, R. V. 1966 Thermocapillary convection in horizontal layer of liquid. *J. Appl. Mech. Tech. Phys.* **7**, 43.

Boeck, T. 2000 Bénard-Marangoni convection at low Prandtl numbers – Results of direct numerical simulations. PhD thesis, Ilmenau Technical University.

Canuto, C., Hussaini, M., Quarteroni, A. & Zhang, T. 1987 *Spectral Methods in Fluid Dynamics.* Springer.

Colinet, P., Legros, J. C. & Velarde, M. G. 2001 *Nonlinear Dynamics of Surface-Tension-Driven Instabilities.* Wiley.

Davis, S. H. 1987 Thermocapillary instabilities. *Annu. Rev. Fluid Mech.* **19**, 403.

Hosoi, A. E. & Bush, W. M. 2001 Evaporative instabilities in climbing films. *J. Fluid Mech.* **442**, 217.

Kelly, R. E. 1994 The onset and development of thermal convection in fully 'developed shear flows. *Adv. Appl. Mech.* **31**, 35–112.

Kuhlmann, H. C. 1999 *Thermocapillary Convection in Models of Crystal Growth.* Springer.

Malomed, B. A., Nepomnyashchy, A. A. & Nuz, A. E. 1994 Nonequilateral hexagonal patterns. *Physica* D **70**, 357.

Nepomnyashchy, A. A., Simanovskii, I. B. & Braverman, L. M. 2001*a* Stability of thermocapillary flows with inclined temperature gradient. *J. Fluid Mech.* **442**, 141.

Nepomnyashchy, A. A., Velarde, M. G. & Colinet, P. 2001*b* *Interfacial Phenomena and Convection.* Chapman & Hall/CRC.

Nitschke, K. & Thess, A. 1995 Secondary instability in surface-tension-driven Bénard convection. *Phys. Rev.* E **52**, R5772.

Palm, E. 1960 On the tendency towards hexagonal cells in steady convection. *J. Fluid Mech.* **19**, 183.

Parmentier, P. M., Regnier, V. C. & Lebon, G. 1993 Buoyant-thermocapillary instabilities in medium-Prandtl-number fluid layers subject to a horizontal temperature gradient. *Intl J. Heat Mass Transfer* **36**, 2417.

Pearson, J. R. A. 1958 On convection cells induced by the surface tension. *J. Fluid Mech.* **4**, 489.

Priede, J. & Gerbeth, G. 1997 Convective, absolute and global instabilities of thermocapillary-buoyancy convection in extended layers. *Phys. Rev.* E **56**, 4187.

Scanlon, J. W. & Segel, L. A. 1967 Finite amplitude cellular convection induced by surface tension. *J. Fluid Mech.* **29**, 149.

Smith, M. K. & Davis, S. H. 1983*a* Instabilities of dynamic thermocapillary liquid layers. Part 1. Convective instabilities. *J. Fluid Mech.* **132**, 119.

Smith, M. K. & Davis, S. H. 1983*b* Instabilities of dynamic thermocapillary liquid layers. Part 2. Surface-wave instabilities. *J. Fluid Mech.* **132**, 145.

Smith, M. K. 1986 Instabilities mechanisms in dynamic thermocapillary liquid layers. *Phys. Fluids* **29**, 3182.

Smith, M. K. 1988 The nonlinear stability of dynamic thermocapillary liquid layers. *J. Fluid Mech.* **194**, 391.

Thual, O. 1992 Zero-Prandtl-number convection. *J. Fluid Mech.* **240**, 229.

Ueno, I., Kurosawa, T. & Kawamura, H. 2002 Thermocapillary convection in thin liquid layer with temperature gradient inclined to free surface. In *Heat Transfer 2002, Proc. Twelfth Intl Heat Transfer Conf.* pp. 129–133. Elsevier.

Weber, J. E. 1978 On the stability of thermally driven shear flow heated from below. *J. Fluid Mech.* **87**, 65.

Xu, J. & Zebib, A. 1998 Oscillatory two- and three-dimensional thermocapillary convection. *J. Fluid Mech.* **364**, 187.